NUCLEAR PHYSICS REACTIONS OF ASTROPHYSICAL IMPORTANCE

BY PATRICK D. O'MALLEY

A dissertation submitted to the

Graduate School—New Brunswick

Rutgers, The State University of New Jersey

in partial fulfillment of the requirements

for the degree of

Doctor of Philosophy

Graduate Program in Physics and Astronomy

Written under the direction of

Dr. Jolie Cizewski

and approved by

_____

_____

_____

_____

_____

New Brunswick, New Jersey

May, 2012

ABSTRACT OF THE DISSERTATION

Nuclear Physics Reactions of Astrophysical Importance

by Patrick D. O'Malley

Dissertation Director: Dr. Jolie Cizewski

Understanding the origin of elements in the universe is one of the main goals of nuclear science and astrophysics today. Achieving this goal involves determining how the elements and their isotopes formed and being able to predict their abundances. At the Holifield Radioactive Ion Beam Facility (HRIBF) at Oak Ridge National Laboratory (ORNL), an experimental program has been established to use transfer reactions (such as (p,d) or (d,p)) to study the properties of many nuclei important to understanding the origins of various elements. Three measurements were done to aid in the determination of the origins of different light isotopes.

Big Bang Nucleosynthesis calculations, constrained by the Wilkinson Microwave Anisotropy Probe results, produce primordial ^{7}Li abundances almost a factor of four larger than those extrapolated from observations. Since primordial ^{7}Li is believed to be mostly produced by the beta decay of ^{7}Be, one proposed solution to this discrepancy is a resonant enhancement of the $^{7}\mathrm{Be}(d,p)2\alpha$ reaction

rate through the $5/2^+$ 16.7-MeV state in ^{9}B. The ^{2}H(^{7}Be,d)^{7}Be reaction was used to search for such a resonance; none was observed. An upper limit on the width of the proposed resonance was deduced.

^{19}F is believed to have formed in Asymptotic Giant Branch stars, but current models cannot reproduce the observed abundances of this nucleus. One of the key reactions responsible for the creation of ^{19}F is ^{15}N(α,γ). Therefore, it is important to understand reactions that might destroy ^{15}N, such as ^{15}N(n,γ). The magnitude of the ^{15}N(n,γ) reaction rate depends directly on the neutron spectroscopic factors of low-lying ^{16}N levels. Currently the measured spectroscopic factors differ from those expected from theory by a factor of 2. A study has been done to resolve this discrepancy using the d(^{15}N,p) reaction. The spectroscopic factors were all found to be close to unity which is in agreement with theoretical predictions.

In novae, gamma ray emission is believed to be primarily due to electron-positron annihilation, though the source of these positrons remains a mystery. The positrons are believed to originate from the beta decay of ^{18}F due to its long half-life ($t_{1/2} \sim 110$ min.). To date, gamma rays from this nucleus have not been observed. Therefore, studies have been made on reactions believed to destroy ^{18}F, such as ^{18}F(p,α) which goes through states in ^{19}Ne. A recent study by Adekola *et al.* showed that a state at 6.289-MeV in ^{19}Ne, just below the proton threshold, could have a significant impact on this reaction rate. However, the spin of this state could not be determined. To determine the spin of this sub-threshold state, a study of the ^{20}Ne(p,d) reaction was made using a proton beam on a carbon foil implanted with ^{20}Ne. Due target contaminants, a spin assignment could not be made, but a new experimental design was created and is described in this dissertation.

Acknowledgements

At this point in my life, I must look back and realize "wow, I've spent 82.14(17)% of my life in school working towards this point." It is hard to summarize exactly how much help that I have received to get here and harder still to express my gratitude. However, the life of an nuclear experimentalist is filled with difficult tasks so I can not make it a habit of allowing that to stop me.

I'd like to start by thanking Jolie Cizewski, my adviser. It was she who convinced me to attend Rutgers, rather than take a year off between undergraduate and graduate school. Jolie's persistence convinced me and without her support and encouragement over these past few years I would not have made it this far. She has also taught me what it means to be a professional.

Next I need to thank my family. My parents, who have moved me across the country more times than I can even count. They were ceaseless in their support and encouragement and despite the fact that they have no idea what I do, they still try to explain it to their friends. My brother and sister for keeping me informed of family matters so that I would feel like I was still involved. My grandparents from both sides of my family, who taught me at an early age to finish what I begin. I'd like to thank my Aunt Terri, who actually gave me her car for an entire summer. My Uncle Scott and Aunt Jean, who welcomed me into their home on Long Island to decompress after particularly stressful weeks.

I also need to thank the entire astrophysics group at Oak Ridge National Laboratory (ORNL). They have quite literally taught me almost everything I know about low energy nuclear physics. I'd like to thank Dan Bardayan for

allowing me to frequently ask him questions with obvious answers and to raid his office for candy and whoopi cakes. Steve Pain also has my gratitude, as much for his dry british wit as for all that he has taught me. Michael Smith for showing me how tirelessly group leaders work to ensure that we can keep doing measurements such as the ones presented in this dissertation. I thank Ray Kozub and John Shriner who guided my undergraduate education and introduced me to nuclear physics in the first place.

Thanks go to Bill Peters for his ever "inspiring" jokes that have only been topped by Brian Moazen's brick joke, which grows longer and more complicated with each telling. I'd like to thank Stan Paulauskas, Miguel Madurga, and Stephen Padgett for our memorable trips to Barleys to show me that physicists DO know how to have a good time. I'd like to thank Stephen Pittman, who's love of food rivals my own. Also thank you Kelly Chipps for allowing me to frequently vent my frustrations in her office. Thanks also to Andy Chae and Milan Matos for all their advice about where I need to go from here. Furthermore, thanks to Carl Gross, Dan Stracener, and all operators at ORNL for actually producing the beams necessary for these measurements.

Finally I want to thank my committee members, who are the unfortunate ones that must read and critique this dissertation. I tried to make the reading of this paper as painless as possible for you.

Dedication

I dedicate this dissertation to my wife, Ginger. Without her unfailing support, I am not certain I would have arrived at this point.

Table of Contents

List of Tables

List of Figures

Chapter 1
Introduction

Understanding the origin of elements in the universe is one of the main goals of nuclear science and astrophysics today. In order to accomplish this, we must determine how the elements and their isotopes formed and be able to predict their abundances. Completely solving this problem is beyond the scope of this dissertation, however the work here does help to improve models of how elements formed. Before describing the measurements made for this dissertation, it is necessary to provide some context. This chapter provides a brief introduction to nuclear structure physics and nuclear astrophysics so that the motivations for these measurements might be better understood.

1.1 Nuclear Physics

Low energy nuclear physics is an investigation of nuclear properties and the laws governing the structure of the nucleus. This investigation involves studying both the relative motion of the constituents of the nucleus and their collective motion. Efforts to understand the nucleus have existed since its discovery by Rutherford in his famous experiment in 1909. Over the past century many advances have been made, from the discovery of the neutron to the development of the modern nuclear shell model. Most of this section was adapted from [Kra88].

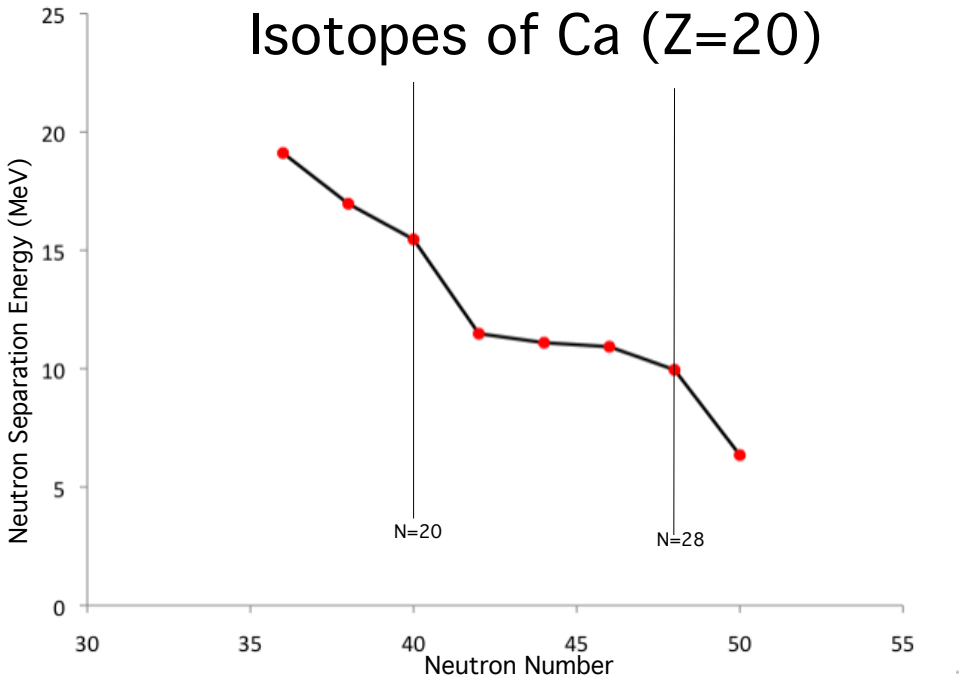

Figure 1.1: Neutron separation energies as a function of neutron number for several even calcium isotopes. Note the sudden drop in separation energy after N=20 and N=28, corresponding to shell closures and a gap in energy levels. Data here are adopted from the NNDC

1.1.1 Shell Model

Atomic theory based on a shell model has helped to clarify the details of atomic structure. Nuclear physicists, having their history in atomic theory, have used the same tool to address the mystery of the structure of the nucleus. However, when making this leap to nuclear physics, several complications arise. Among them is that in the atomic case, the potential supplied to the electrons is 'external' to the electron, originating in the positively charged nucleus. However, in the nucleus, the particles are traveling in a potential that they themselves create. Furthermore, while electrons have an effective size much smaller than that of the atom, nucleons themselves have a size comparable to that of the nucleus as whole.

Despite these difficulties there has been a great deal of scientific evidence

to support the existence of a nuclear shell structure. Figure 1.1 shows neutron separation energies, the energy it takes to remove a neutron from the nucleus, as a function of neutron number for several calcium isotopes. Note how after neutron numbers 20 and 28, there is a sudden drop in separation energies. These sudden drops correspond to the filling of major shells, as in atomic theory. The 'magic' numbers at which these drops occur are the same for both neutrons and protons (i.e. 2, 8, 20, 28, 50, 82, 126). This observation supports the notion that the constituents of the nucleus can be treated as individual particles moving in a potential well.

As a first step, the nuclear potential can be approximated by a harmonic oscillator potential, with each state having a $2(2\ell + 1)$ degeneracy. For the first few states, this theory seems to reproduce the magic numbers (2, 8, 20), but it breaks down at higher levels. As an improvement to this model, a potential should be used that better matches the mass distribution in the nucleus, such as the Woods-Saxon potential (to be discussed later in this dissertation). However, this model, while seemingly appropriate in its design, also does not reproduce the magic numbers. The correction needed was discovered by Mayer, Haxel, Suess, and Jensen in 1949. If a strong spin-orbit attractive interaction is included in the potential, then the magic numbers are reproduced (see Figure 1.2). It should be noted that this spin orbit force, while analogous to the atomic spin orbit force, is not due to an electromagnetic force.

Despite its relative simplicity, the shell model successfully accounts for the spins and parities of states in many nuclei. In these nuclei, the properties of the nucleus can be attributed to the motion of the nucleons in the open valence shells. However, there is little experimental data for weakly-bound nuclei far from the valley of stability where the traditional description of the shell model may not be valid. Due to this lack of data, tests of the shell model in exotic nuclei are

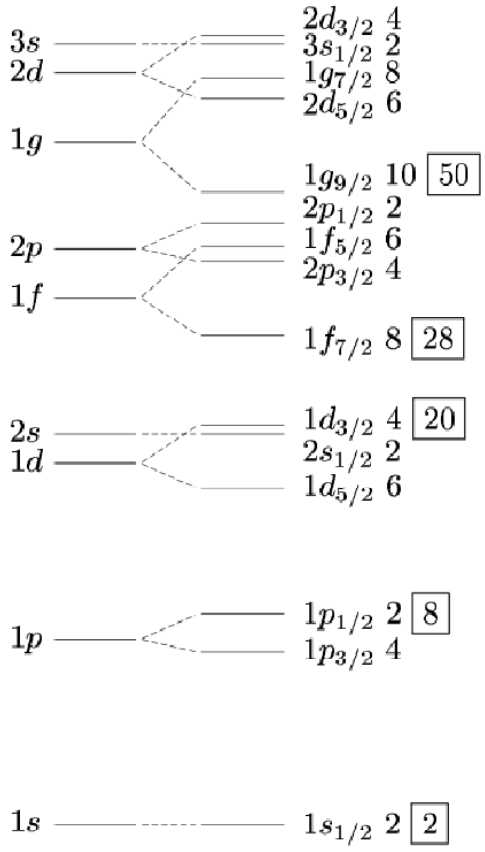

Figure 1.2: To the left are single particle states calculated from Woods-Saxon potential alone. At the right is the same potential including a spin-orbit term in the potential.

currently among the highest priority experiments being performed at radioactive ion beam facilities [Jon10].

1.2 Nuclear Astrophysics

Nuclear astrophysics is, in part, the study of the nuclear processes which drive the birth, evolution, and death of stars. Our current cosmological belief is that the nuclei which make up the majority of matter were first made from nucleons created a short time after the beginning of the Universe, in the expanding fireball

we call the Big-Bang. Nuclei were later forged in the interiors of stars and stellar explosions. In fact, it is one of the primary goals of physicists today to explain the origin and abundance of all the elements (and their isotopes) in the universe.

Tremendous effort has been spent by astrophysicists to model the complicated reactions that occur, both in the big bang and during stellar evolution, to create these nuclei. However, one of the major inputs needed to complete these models is information about the properties of the nuclei involved. This information includes energies and spin-parities of levels, masses, half-lives, and cross sections for key reactions. It is the goal of the nuclear astrophysics experimentalist to measure these quantities which allows more accurate and precise models to be developed. In fact, all of the experiments discussed in this dissertation are of astrophysical importance to address the origins of nuclei. The rest of this chapter will be spent providing some astrophysical background so that the motivations for these measurements might be better understood. The information provided here is adapted from [Ost07].

1.2.1 The Big Bang

A model of big bang model nucleosynthesis (BBN) was proposed in the 1940's to explain the origin and abundance of chemical elements in the universe. This model assumes that the early universe consisted of a very hot, very dense gas that expanded into its current state. Initially the universe existed in a state sometimes called the "cosmic fireball." At this point this "cosmic fireball" was comprised primarily of a dense quark gluon plasma. The temperature was so high that particle anti-particle pairs (primarily leptons and quarks) were continuously being created and destroyed. Eventually, some unknown reaction led to a violation of baryon number and created an excess of matter over antimatter.

The universe continued to expand and cool and at about 10^{-6} s, quarks bonded

to form heavier particles, like protons. While these protons were energetic enough to overcome the repulsive Coulomb barrier, temperatures were too high for fusion to occur since these nuclei would immediately be destroyed by the excess energy brought into the reaction. About 1 second after the initial expansion, conditions would become right for a variety of processes to occur (see Figure 1.3) and lead to the production of many of the light elements (e.g. ^{2}H, ^{3}He, ^{4}He, ^{7}Li).

Throughout the big bang, photons have been interacting with matter with photons creating particle anti-particle pairs or interacting particles creating photons. However, after about 379,000 years, the universe cooled to the point that the radiation decoupled from matter and moved through the universe unimpeded. As such, BBN models also predict a relic background radiation of photons that would permeate the universe. In 1965 a radio telescope measured this radiation for the first time. Eventually the spectrum was determined to peak in the microwave region and corresponded to a black body temperature of around 2.73 K [Pen65]. The big bang model's ability to predict the existent of this cosmic microwave background (CMB) is considered to be one of its greatest strengths and therefore much work has been done over the past 50 years to improve the big bang model.

BBN models are used for abundance calculations of light elements as a function of several parameters. They are particularly sensitive to the Hubble constant H_0 (often expressed in its dimensionless form $h = \frac{H_0}{100\ km\ s^{-1}\ Mpc^{-1}}$) and the cosmological baryon density parameter, $\Omega_b \equiv \frac{\rho_b}{\rho_c}$ where ρ_b is the baryonic mass density and ρ_c is the critical density at which the universe is spatially flat. The CMB carries with it a record of the conditions of the Universe at the point in which neutral atoms formed, at which time the baryons became transparent to photonic radiation. Therefore, oscillations in temperature in different parts of the microwave sky tell us about the conditions in the universe close to the time of the

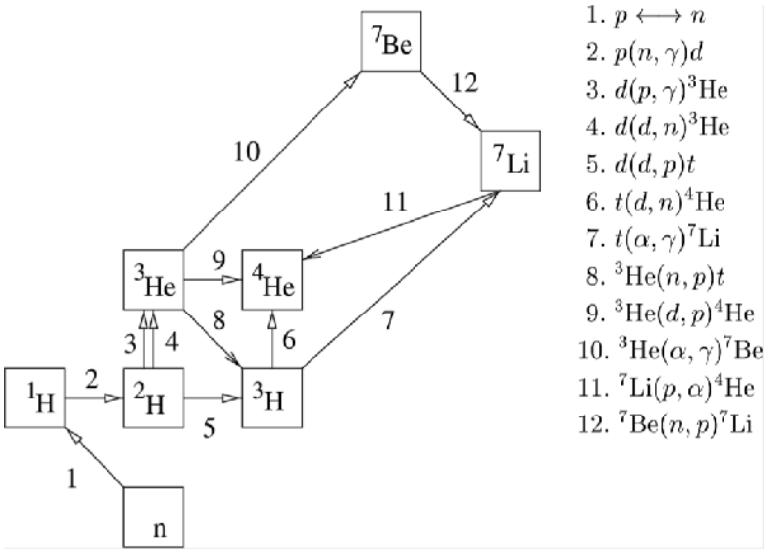

Figure 1.3: Various reactions in standard BBN simulators to produce light isotopes during the big bang. [Bru11]

Big Bang. Recently NASA's Wilkinson Microwave Anisotropy Probe (WMAP) performed a precise mapping of these temperature anisotropies. This study led to a measure of h and Ω_b to unprecedented precision [Spe03]:

$$h = 0.705 \pm 0.013 \tag{1.1}$$

$$\Omega_b h^2 = 0.0227 \pm 0.0006 \tag{1.2}$$

The baryonic density parameter is more commonly expressed as η, the baryon to photon ratio ($\eta = 6.2 \pm 0.2 \times 10^{-10}$.

1.2.2 Star birth

In the interstellar medium, there exist giant clouds of molecular hydrogen and helium. Typically the cores of these clouds tend to be very cold ($\approx$ 10 K). However, if gravitational collapse is triggered (often by a shock wave from a nearby nova or supernovae), the temperature will begin to rise due to the conversion of

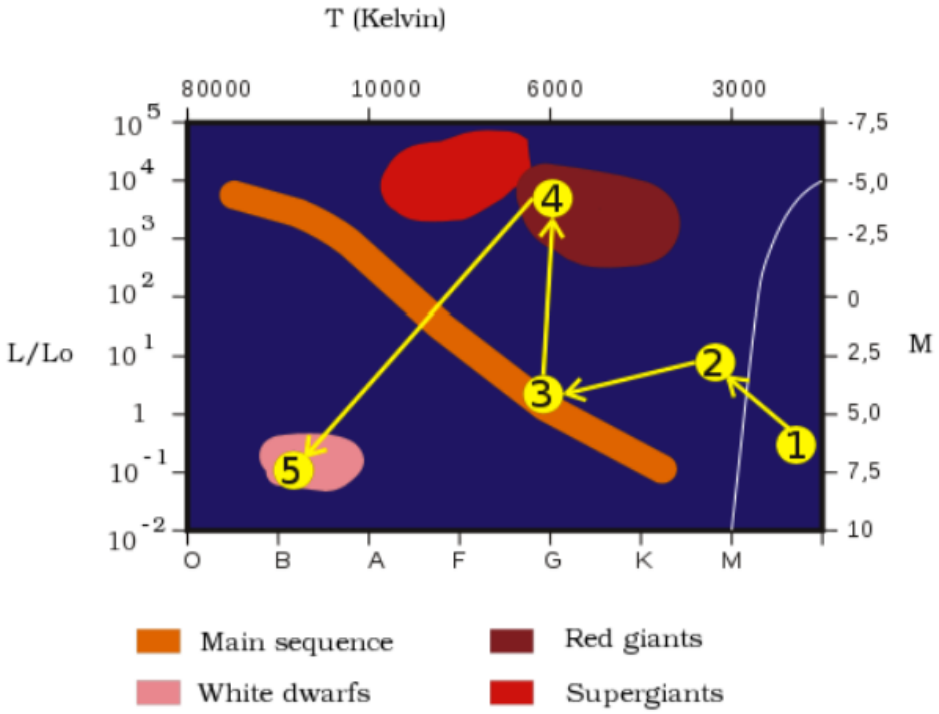

Figure 1.4: Hertzsprung-Russell (HR) diagrams are plots of a stars luminosity (light output) or mass as a function of its temperature. This HR diagram demonstrates the evolution of a star in 5 stages. (1) The star begins as a molecular cloud of hydrogen and helium. (2) The cloud collapses into protostar. (3) Star is undergoing hydrogen fusion in the core and is now a main sequence star. (4) Hydrogen shell burning forces the start to expand into a Red Giant. (5) The star sheds its outer layers and forms a white dwarf. Figure taken from [Wiki]

gravitational potential energy into thermal energy. Initially most of this heat is lost as radiation, but once the cloud becomes dense enough to become opaque to radiation (now called a protostar), the temperature will rise rapidly.

After this gravitational collapse is triggered, the protostar will continue to contract and heat. Once the core region of this star becomes dense and hot enough ($\approx 10^6$ K) the kinetic energy of the hydrogen and helium nuclei are such that they can overcome the Coulomb barrier. This enables fusion reactions to occur, releasing a huge amount of energy. The radiation pressure in the core is sufficient to balance the inward force of gravity and the star reaches hydrostatic

equilibrium. At this point the star is considered to be on the *Main Sequence* where it spends the majority of its life. Figure 1.4 shows a simplified Hertzsprung-Russell (HR) diagram demonstrating the evolution of a star. HR diagrams are plots of a star's luminosity (light output) or mass as a function of its temperature and are a useful tool for astrophysicists to display and interpret observations.

1.2.3 Hydrogen burning

While a star is on the main sequence, the thermonuclear reactions that provide most of its power in the core are part of the proton-proton chain (pp chain). This chain occurs in 3 stages:

$${}^{1}_{1}H + {}^{1}_{1}H \rightarrow {}^{2}_{1}H + e^{+} + \nu_e$$

$${}^{2}_{1}H + {}^{1}_{1}H \rightarrow {}^{3}_{2}He + \gamma$$

$${}^{3}_{2}He + {}^{3}_{2}He \rightarrow {}^{4}_{2}He + p + p$$

An alternative path exists for the conversion of hydrogen into helium called the CNO cycle. Here carbon, nitrogen, and oxygen are used as the catalysts for the fusion reactions.

$${}^{12}_{6}C + {}^{1}_{1}H \rightarrow {}^{13}_{7}N + \gamma$$

$${}^{13}_{7}N \rightarrow {}^{13}_{6}C + e^{+} + \nu_e$$

$${}^{13}_{6}C + {}^{1}_{1}H \rightarrow {}^{14}_{7}N + \gamma$$

$${}^{14}_{7}N + {}^{1}_{1}H \rightarrow {}^{15}_{8}O + \gamma$$

$${}^{15}_{8}O \rightarrow {}^{15}_{7}N + e^{+} + \nu_e$$

$${}^{15}_{7}N + {}^{1}_{1}H \rightarrow {}^{12}_{6}C + {}^{4}_{2}He$$

The energy output from this reaction cycle is much more strongly dependent on temperature than the pp chain. With T_6 being the temperature in MK, the CNO energy output scales as $T_6^{19.9}$ rather than T_6^4 as is the case for the pp chain. However, as the protostar must have been previously enriched in CNO nuclei for

this cycle to be possible, so that the pp chain is still the dominating reaction for most main sequence stars. For very massive stars, the CNO cycle is the primary mechanism for fusion in the core.

1.2.4 Later Evolution

Eventually a star's hydrogen fuel will be exhausted in the core. When this happens, a layer of hydrogen around the core will ignite and burn its way outward, depositing more helium ash onto the core. This shell burning causes the core to contract and heat up. At this point, the hydrogen burning shell begins heating the outer layers of the star causing them to expand. This is called the *red giant phase*. Once the temperature reaches $\approx 10^8$ K, helium burning starts in the core through the triple alpha process, converting the helium into carbon.

$${}^4_2He + {}^4_2He \rightarrow {}^8_4Be + \gamma$$

$${}^8_4Be + {}^4_2He \rightarrow {}^{12}_6C + \gamma$$

If the star has a mass on the order of 1 solar mass or greater, once the helium in the core has been exhausted, the core contracts again and a similar envelope of expansion occurs as with the red giant phase. The star has entered into its Asymptotic Giant Branch (AGB) stage and will undergo a period of intermittent hydrogen shell burning and helium shell burning. Eventually though, the outer layers are thrown off into the interstellar medium and what remains is a dense degenerate star called a *white dwarf*, composed mostly of carbon and oxygen. A degenerate system is one in which the electrons are forced into the lowest energy levels, getting stacked into progressively higher and higher levels. In degenerate stars, the pressure opposing gravity is primarily due to the Pauli-Exclusion principle instead of thermal pressure described by the ideal gas law. It should be kept in mind though that a white dwarf is not truly a star since all nuclear reactions have ceased.

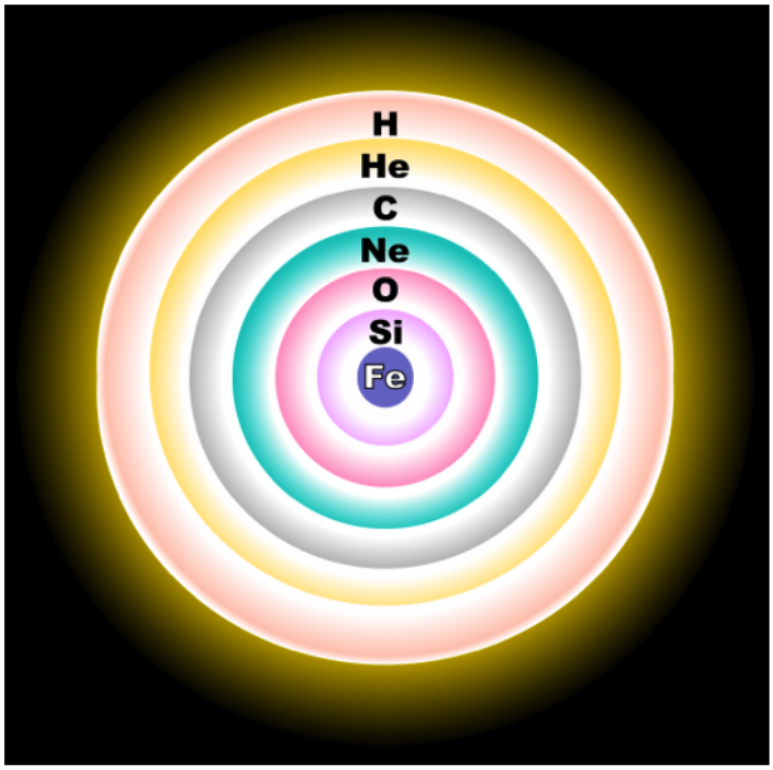

Figure 1.5: Each layer of this star represents a layer of fusion burning that can occur for very massive stars. (The hydrogen layer burns into helium, the helium layer burns into carbon, etc). [Wiki]

Heavier stars can undergo even further conversions similar to the triple alpha process before becoming white dwarfs. These later stages convert carbon, oxygen, and for heavier stars even silicon into heavier elements. Figure 1.5 demonstrates the various burning layers that very heavy stars can achieve. However, once the core becomes primarily composed of Fe ash, fusion will cease, as fusion would no longer be energetically favorable due to the high binding energy per nucleon of Fe. Particularly massive stars can undergo a violent ending to their lives as supernovae (with cores 1.4 solar masses), distributing heavy elements into the interstellar medium to become components of new stars.

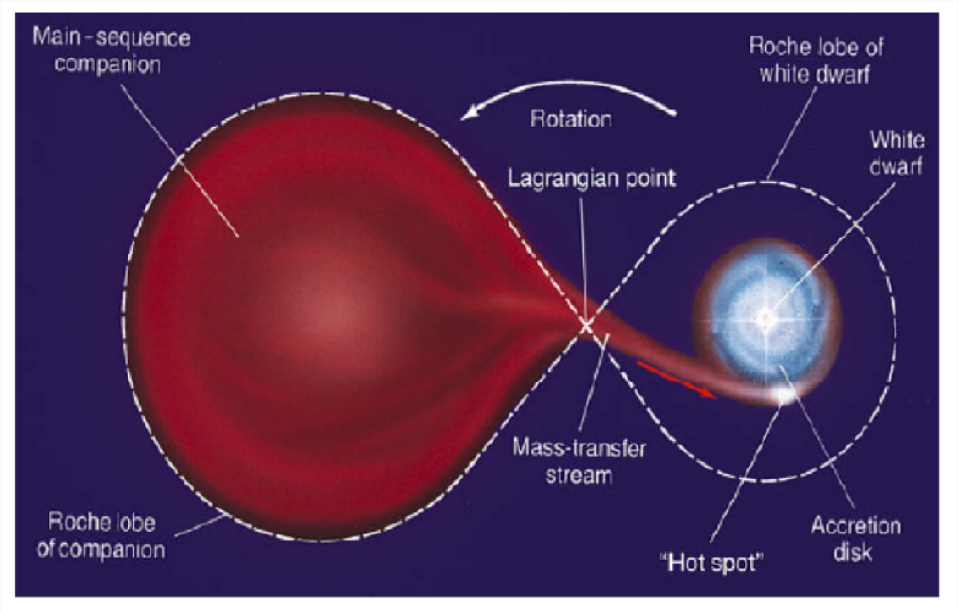

Figure 1.6: When a star overflows its Roche Lobe the matter is no longer bound to the star, thus enabling the accretion of matter onto the white dwarf. [Wiki]

1.2.5 Novae

Viewing the universe from earth, it is tempting to conclude that single stars like the Sun are typical. However, roughly half of all stars are actually systems of multiple stars, occurring often in binary systems. In some of these binary systems, one of the stars is a white dwarf. Often the stars' gravitational fields overlap, and one star will accumulate hydrogen and/or helium gradually from its companion star. This matter accretes in a thin layer on the surface of the white dwarf. At low temperatures the equation of state at the surface of the white dwarf is degenerate and the pressure is essentially independent of the temperature.

As matter is deposited and compressed on the surface of the white dwarf, the temperature in this accumulating layer rises. Thermonuclear reactions can be ignited in degenerate matter as the energy of the particles becomes sufficient to overcome the Coulomb barrier. These reactions can cause a thermonuclear

runaway, with the temperature rising until it is sufficient to break the degeneracy, thus increasing the pressure. This pressure blows off the hot burning surface layer, and this sudden explosive burst is called a nova. The typical total energy output from a nova is on the order of 10^{45} erg, a trillion times more energy than the Sun produces each second. Even though the energy output is large, the white dwarf only ejects about 10^{-4} of its mass so nova do not usually destroy the white dwarf. At this point ,the white dwarf usually begins to accrete matter again, making this process cyclic in nature. [Ost07]

1.3 Form of Dissertation

This dissertation is comprised of three measurements done to help understand the origins of different elements. Calculations for post Big Bang ^{7}Li abundances differ from abundances extrapolated from observations by almost a factor of 4 [Spe03]. Primordial ^{7}Li is believed to be mostly produced by the beta decay of ^{7}Be. One of the proposed solution to this discrepancy is a resonant enhancement of the $^{7}\mathrm{Be}(d,p)2\alpha$ reaction rate through the $5/2^{+}$ 16.7-MeV state in ^{9}B [Cyb08]. The $^{2}\mathrm{H}(^{7}\mathrm{Be},d)^{7}\mathrm{Be}$ reaction was used to search for such a resonance.

It is believed that ^{19}F is formed in Asymptotic Giant Branch stars, which are stars with inert carbon cores with a shell of helium burning and a shell of hydrogen burning. However the observed abundances of this nucleus are not reproduced by current models [Lug04]. $^{15}\mathrm{N}(\alpha,\gamma)$ is believed to be the primary mechanism for the creation of ^{19}F. The magnitude of the $^{15}\mathrm{N}(n,\gamma)$ reaction rate is important because it would directly affect the $^{15}\mathrm{N}(\alpha,\gamma)$ reaction rate by removing ^{15}N from the system. This rate depends directly on the neutron spectroscopic factors of low-lying ^{16}N levels. Currently measured spectroscopic factors and those expected from theory differ by a factor of 2 [Mei96, Boh72, Lee07]. A study has been done

to resolve this discrepancy using the $^{15}\mathrm{N}(d,p)$ reaction.

Gamma ray emission in novae is believed to be due to electron-positron annihilation. It is believed that the positrons originate from the beta decay of long-lived $^{18}\mathrm{F}$ ($t_{1/2} \sim 110$ min.). However to date, gamma rays from this nucleus have not been observed [Ber02, Koz06, Ser07]. A recent study by [Ade11] showed that a state at 6.289-MeV, just below the proton threshold, could have a significant impact on the $^{18}\mathrm{F}(p,\alpha)$ reaction rate, a reaction believed to be responsible for the destruction of $^{18}\mathrm{F}$. In this measurement, the spin of this state could not be determined. To determine the spin of this sub-threshold state, the $^{20}\mathrm{Ne}(p,d)$ reaction was studied using a proton beam on a carbon foil implanted with $^{20}\mathrm{Ne}$.

Although all are nuclear astrophysics measurements, the motivations and techniques of each experiment of this dissertation are different. Rather than address all theoretical and experimental needs for each experiment separately, the next two chapters will be devoted to discussing the theoretical tools that allow experimentalists to interpret their data, as well discuss the laboratory tools that make such measurements possible. Following the instrumentation chapter, the individual experiments will be discussed in separate chapters, each with their own motivation and analysis. Finally, in the last chapter the results of these efforts will be summarized and future goals for this research are presented.

Chapter 2

Theory

Each of the measurements of this dissertation were nuclear physics reactions. In each reaction, it is particle energies, cross sections, and angular distributions that are actually measured. From these data, characteristics of nuclear states like the spins or spectroscopic factors were determined. However, to make these determinations, a theoretical frame work is needed to interpret the data. Specifically, the goal of any reaction theory is to describe the transition of the system from an initial state (particles a and A) to the final state (particles b and B) and to use this description to derive expected cross sections. This chapter aims to describe the theoretical nuclear models and tools used to interpret the results of the measurements of this dissertation. However, since most each of the measurements of this dissertation are motivated by a desire to improve models of astrophysical reactions, we shall begin with a discussion of reaction rates, adopted from [Rol88].

2.1 Thermonuclear Reaction Rates

In stellar environments, nuclear material is synthesized when two or more nuclei interact to form a new species. In order to create nucleosynthesis models, it is necessary to understand the rates of the various reactions involved. In order to calculate these reactions rates, the probability, or cross section, that the reaction will occur needs to be known. Consider two particles with charges Z_A and Z_B, masses m_A and m_B, and number densities N_A and N_B. With v defined as the

relative velocity between these two particles and $\sigma(v)$ giving the probability that this reaction will occur, the reaction rate can is defined as

$$R_{AB} = N_A N_B v\sigma(v) \tag{2.1}$$

For a star at temperature T, the relative velocity v varies over a large range of values given by the Boltzmann distribution

$$\phi(v) = 4\pi v^2 \left(\frac{m_r}{2\pi kT}\right)^{3/2} exp\left(-\frac{m_r v^2}{2kT}\right) \tag{2.2}$$

where m_r is the reduced mass. For simplicity one one pair of particles will be considered now since reaction rates depend linearly on the number densities of A and B. Remembering $E = \frac{1}{2}mv^2$, the reaction rate can be written as

$$< \sigma v >= \int_0^\infty \phi(v)v\sigma(v)dv = \left(\frac{8}{\pi m_r}\right)^{1/2} (kT)^{-3/2} \int_0^\infty E\sigma(E)exp\left(-\frac{E}{kT}\right) dE. \tag{2.3}$$

So now it is necessary to come up with an expression for the cross section $\sigma(E)$. Nuclear interactions only occur over distances on the order of fm (10^{-15} m). However, the Coulomb force repelling the two particles acts over a much longer distance. The distance of closest approach, r_C, corresponds to the point where the potential energy reaches that of the initial energy of the approaching particle, E.

$$E = \frac{Z_A Z_B e^2}{4\pi\epsilon_0 r_C} \tag{2.4}$$

Classically, fusion would only be possible if nucleons had enough energy to overcome this Coulomb Barrier. E_C (i.e. $r_C \approx$ fm). For r_C on the order fm, the Coulomb Barrier is on the order of MeV. For most stellar environments, the average kinetic energy of the nuclei, kT is on the order of keV. However, according to quantum mechanics, there is a probability to penetrate this Coulomb barrier by *quantum tunneling*. This tunneling occurs with a characteristic energy-dependent probability called the *Penetrability*, P_ℓ and is given by

$$P_\ell = \frac{\kappa r}{F_\ell^2 + G_\ell^2} \tag{2.5}$$

where κ is the wave number, r is the separation between A and B, and F_ℓ and G_ℓ are the regular and irregular solutions to the Coulomb wavefunction for a given relative orbital angular momentum ℓ. For energies much lower than the Coulomb barrier, this penetrability can be approximated as

$$P \approx exp\left[-\left(\frac{E_G}{E}\right)^{1/2}\right] \tag{2.6}$$

Here E_G is called the *Gamow* energy and is given by $E_G = (\pi\alpha Z_A Z_B)^2 2m_r c^2$, where $\alpha \approx 1/137$ is the fine structure constant.

The cross section for this reaction depends directly this penetrability, as well a geometric factor $1/E$ to account for the "size" of the nucleus. Therefore the cross section can be written as.

$$\sigma(E) = E^{-1} exp\left[-\left(\frac{E_G}{E}\right)^{1/2}\right] S(E) \tag{2.7}$$

The term $S(E)$ is known as the astrophysical S-factor and accounts for the specifically nuclear effects that determine the reaction probability. Now with an expression for the cross section, the reaction rate can be written as

$$< \sigma v >= \left(\frac{8}{\pi m_r}\right)^{1/2} (kT)^{-3/2} \int_0^\infty S(E) exp\left(-\frac{E}{kT} - \frac{E_G}{E^{1/2}}\right) dE. \tag{2.8}$$

It is typically very difficult to measure the cross sections at astrophysical energies ($E \approx$ keV). However, $S(E)$ is a smooth slowly varying function of energy when resonances aren't present. As such, it is often the practice to measure cross sections at higher energies, extract the S-factor, and then extrapolate this factor to lower energies. As such the remainder of this chapter will be devoted to deriving frameworks in which experimental cross sections can be determined.

2.2 Direct Reactions

Direct nuclear reactions (taking place over time $\approx 10^{-22}$ s) involve only a few nucleons on the surface of the nucleus, or only the nucleus as a collective whole. In these reactions the system goes from initial partition α (A+a) to partition β (B+b) (often written as A(a,b)B) directly, meaning there is no intermediate state in between. These tend to occur at higher energies since the reaction is finished quickly and fewer internal collisions are possible. These reactions are strongly influenced by the initial direction of the incoming particles; therefore the cross sections will peaked at low $\theta_{c.m.}$. It is the goal of this section to describe a framework for modeling these reactions. Except where noted, the derivations and notation are adapted from [Sat83].

2.2.1 Cross Sections

For initial partition α, the wave function ψ_α is given as the product of the internal states of the two nuclei,

$$\psi_\alpha(x_\alpha) \equiv \psi_a(x_a)\psi_A(x_A) \tag{2.9}$$

where x_i denotes the internal variables. The states ψ_i are the eigenfunctions of the internal Hamiltonians H_i with corresponding eigenvalues ϵ_i with $H_\alpha = H_a + H_A$ and $\epsilon_\alpha = \epsilon_a + \epsilon_A$. The kinetic energy E_α can be expressed in terms of the total energy E and the internal energies ϵ_α:

$$E_\alpha = E - \epsilon_\alpha \tag{2.10}$$

The total wave function Ψ_α for the system obeys the complete Schrödinger equation $(E - H)\Psi_\alpha = 0$, where $H = H_\alpha + K_\alpha + V_\alpha$ and H_α is the internal

hamiltonians of partition α. Ψ_α can be expanded in terms of any complete set of internal states of partition β:

$$\Psi_\alpha = \sum_\beta \xi_\beta(r_\beta)\psi_\beta(x_\beta). \tag{2.11}$$

The coefficients ξ_β are the projections of Ψ_α onto channels β, describing the relative motion in the channel β. They should have the asymptotic form

$$\xi_\beta(r_\beta) \sim e^{i\mathbf{k}_\alpha\cdot\mathbf{r}_\alpha}\delta_{\alpha\beta} + f_{\beta\alpha}(\hat{\mathbf{k}}_\beta, \mathbf{k}_\alpha)\frac{1}{\mathbf{r}_\beta}e^{ik_\beta r_\beta}. \tag{2.12}$$

Here $\mathbf{k}_i$ is the wave number for the channel i and $\hat{\mathbf{k}}_i$ is a unit vector long $\mathbf{k}_i$. This equation defines the scattering amplitude $f_{\beta\alpha}$ as the amplitude of the outgoing spherical wave in channel β scattered from an incoming plane wave of unit amplitude in channel α. If $\alpha = \beta$, then $f_{\beta\alpha}$ describes either elastic ($f_{\alpha\alpha}$) or inelastic ($f_{\alpha'\alpha}$) reactions. Often a transition amplitude is used and is found by re-normalizing the scattering amplitude.

$$T_{\beta\alpha} = -\frac{2\pi\hbar^2}{\mu_\beta}f_{\beta\alpha} \tag{2.13}$$

where μ_β is the reduced mass of partition β. So the differential cross section for the transition $\alpha \to \beta$ is given by

$$\frac{d\sigma_{\beta\alpha}}{d\Omega} = \frac{\mu_\alpha\mu_\beta}{(2\pi\hbar^2)^2}\left(\frac{k_\beta}{k_\alpha}\right)|T_{\beta\alpha}(\mathbf{k}_\beta, \mathbf{k}_\alpha)|^2 \tag{2.14}$$

An expression for the transition amplitude can be obtained from the Schrödinger equation using the appropriate form of H,

$$(E - H_\beta - K_\beta)\Psi_\alpha = V_\beta\Psi_\alpha \tag{2.15}$$

and projecting onto the β channel. This is done by multiplying the above equation from the left by $\psi^*_\beta(x_\beta)$ and integrating over x_β yielding an equation for ξ_β

$$(E_\beta - K_\beta)\xi_\beta(\mathbf{r}_\beta) = (\psi_\beta|V_\beta|\Psi_\alpha) = \int \psi^*_\beta(x_\beta)V_\beta(\mathbf{r}_\beta, x_\beta)\Psi_\alpha dx_\beta. \tag{2.16}$$

It should be noted that projections using parentheses like the equation above imply an integration only over the internal variables x, but the use of bra and ket (i.e. $\langle|\rangle$ implies an integration over all variables. This is the notation adopted from [Sat83] and I will be consistent with his methods. Equation 2.16 remains a function of $\mathbf{r}_\beta$, but it may be solved formally using Green's function techniques:

$$\xi_\beta(\mathbf{r}_\beta) = e^{i\mathbf{k}_\alpha\cdot\mathbf{r}_\alpha}\delta_{\alpha\beta} - \left(\frac{\mu_\beta}{2\pi\hbar^2}\right)\int \frac{e^{ik_\beta|\mathbf{r}_\beta - \mathbf{r}'_\beta|}}{|\mathbf{r}_\beta - \mathbf{r}'_\beta|}(\psi_\beta|V_\beta|\Psi_\alpha)dx_\beta \tag{2.17}$$

In the limit of $r_\beta \gg r'_\beta$, $|\mathbf{r}_\beta - \mathbf{r}'_\beta| \approx r_\beta - \hat{\mathbf{k}}\cdot\mathbf{r}'_\beta$. Using equation 2.12. the transition amplitude becomes

$$T_{\beta\alpha}(\mathbf{k}_\beta, \mathbf{k}_\alpha) = \int\int e^{i\mathbf{k}_\beta\cdot\mathbf{r}'_\beta}\psi^*_\beta(x_\beta)V_\beta(x_\beta, \mathbf{r}'_\beta)\Psi_\alpha(\mathbf{k}_\alpha)dx_\beta d\mathbf{r}'_\beta = \left\langle e^{i\mathbf{k}_\beta\cdot\mathbf{r}'_\beta}|V_\beta|\Psi_\alpha(\mathbf{k}_\alpha)\right\rangle. \tag{2.18}$$

2.2.2 Distorted Wave Born Approximation

Equation 2.18 does not provide a practical solution of the scattering problem, as it still involves a currently unknown total wave function Ψ. An auxiliary potential can be introduced that will not change the internal states of the β partition because it only depends on the channel radius r_β. This implies,

$$[E_\beta - K_\beta - U_\beta(r_\beta)]\xi_\beta(\mathbf{r}_\beta) = (\psi|W_\beta|\Psi_\alpha) \tag{2.19}$$

where W_β is the residual interaction and is given by $W_\beta = V_\beta(x_\beta, \mathbf{r}_\beta) - U_\beta(r_\beta)$. Although the choice of U_β is arbitrary in principle, it is often chosen such that it includes a large part of the average of V_β. Doing so ensures that W_β is small

and can be treated as a perturbation. In fact, U_β is often chosen to be complex so that absorption effects can be taken into account. If the auxiliary potential is chosen such that $U_\beta(r_\beta) = (\psi_\beta|V_\beta|\psi_\beta)$, then the formal solution to the above equation can be expressed in terms of the homogeneous equation

$$[E_\beta - K_\beta - U_\beta(r_\beta)]\chi_\beta^{(+)}(\mathbf{k}_\beta, \mathbf{r}_\beta) = 0 \tag{2.20}$$

These $\chi_\beta^{(+)}$ are the distorted waves and describe the elastic scattering of b on B due to the potential U_β. The time inverse of these functions ($\chi_\beta^{(-)}(\mathbf{k}, \mathbf{r}) = \chi_\beta^{(+)*}(-\mathbf{k}, \mathbf{r})$) are also needed. They are solutions to the equation

$$[E_\beta - K_\beta - U_\beta^*(r_\beta)]\chi_\beta^{(-)}(\mathbf{k}_\beta, \mathbf{r}_\beta) = 0. \tag{2.21}$$

Utilizing Green's function techniques, the transition amplitude takes the form

$$\begin{gathered} T_{\beta\alpha}(\mathbf{k}_\beta, \mathbf{r}_\beta) = T_{\beta\alpha}^{(0)}(\mathbf{k}_\beta, \mathbf{r}_\beta)\delta_{\alpha\beta} + \left\langle \chi_\beta^{(-)}(\mathbf{k}_\beta)\psi_\beta|W_\beta|\Psi_\alpha(\mathbf{k}_\alpha)\right\rangle = \\ T_{\beta\alpha}^{(0)}(\mathbf{k}_\beta, \mathbf{r}_\beta)\delta_{\alpha\beta} + \\ \int\int \chi_\beta^{(-)*}(\mathbf{k}_\beta, \mathbf{r}_\beta)\psi_\beta^*(x_\beta)[V_\beta(x_\beta, \mathbf{r}_\beta) - U_\beta(r_\beta)]\Psi_\alpha(\mathbf{k}_\alpha)dx_\beta dr_\beta \end{gathered} \tag{2.22}$$

So far these forms provide what are called *post* representations of the transition amplitude because it is the interaction V_β or W_β in the final channel that appears. Equations governing nuclear structure are believed to be time-invariant so that the transition amplitude for the reaction $A(a,b)B$ should be the same as that for $B(b,a)A$ up to a phase factor. All these equations could have been derived in the *prior* representations with the potentials V_β or W_β describing the entrance channel. This is important because in the *prior* representation, the equivalent to equation 3.12 would generate distorted waves for the entrance channel $\chi_\alpha^{(+)}(\mathbf{k}_\alpha)$

Ψ_α is expanded in a Born series, and the first term (the elastic part) is assumed to be the most important part. The total wave function can then be approximated as:

$$\Psi_\alpha^{(+)} \approx \chi_\alpha^{(+)}(\mathbf{r}_\alpha)\psi(x_\alpha) \tag{2.23}$$

Therefore the transition amplitude can be expressed as

$$\begin{aligned} T_{\beta\alpha}(\mathbf{k}_\beta, \mathbf{k}_\alpha) = \left\langle \chi_\beta^{(-)}(\mathbf{k}_\beta)\psi_\beta | W | \chi_\alpha^{(+)}(\mathbf{k}_\alpha)\psi_\alpha \right\rangle = \\ \int\int \chi_\beta^{(-)*}(\mathbf{k}_\beta, \mathbf{r}_\beta)(\psi_\beta|W|\psi_\alpha)\chi_\alpha^{(+)}(\mathbf{k}_\alpha, \mathbf{r}_\alpha) d\mathbf{r}_\alpha d\mathbf{r}_\beta \end{aligned} \tag{2.24}$$

and consequently the differential cross section can be expressed as:

$$\frac{d\sigma_{\beta\alpha}^{DWBA}}{d\Omega} = \frac{\mu_\alpha \mu_\beta}{(2\pi\hbar^2)^2} \frac{k_\beta}{k_\alpha} \frac{|T_{\beta\alpha}|^2}{(2J_A+1)(2J_\alpha+1)} \tag{2.25}$$

where J_i represents the total angular momenta of state i,

The challenge is to select an appropriate auxiliary potential, hopefully one that gives the best fits to experimental cross sections. Often these potentials have negative, imaginary components to account for the fact that there are more reactions occurring than are dealt with using these models. These reactions serve to remove flux from the elastic scattering channel. Potentials of this form are called optical model potentials, since they describe both refraction and absorption in the same way as light passing through a refracting medium.

Typically optical model potentials are given in the Woods-Saxon formulation:

$$\begin{aligned} U(r) = \quad & V_c - V(1+e^{x_0})^{-1} + \left(\tfrac{\hbar}{m_\pi c}\right)^2 V_{so}(l\cdot s)\tfrac{1}{r}\tfrac{d}{dr}(1+e^{x_{so}})^{-1} - \\ & i[W(1+e^{x_W})^{-1} - 4W_D \tfrac{d}{dx_D}(1+e^{x_D})^{-1}] \end{aligned} \tag{2.26}$$

where

$V_c = ZZ'e^2/r, r \geq R_c$ or $V_c = (ZZ'e^2/2R_c)(3 - r^2/R_c^2), r < R_c$

$R_c = r_c A^{1/3}$

$x_i = (r - r_i A^{1/3})/a_i$

$\left(\frac{\hbar}{m_\pi c}\right)^2 = 2.00 \text{ fm}^2$

Here V_C, V, V_{so}, W, and W_D describe the Coulomb, real volume, spin-orbit, and imaginary volume and surface potentials. Typically elastic scattering measurements are used to determine the values of these optical model parameters. Here it is important to remember that the optical model potential should act as an average interaction. Thus, it should vary slowly with changing mass (A), atomic number (Z), and energy (E). Several studies, such as [Loh74] and [Per76], have determined relationships between the parameters and the values of A, Z, and E. This is convenient for situations where the elastic scattering has not been measured. However, these global parameters assume that the nucleus is spherical in shape. For many nuclei (as is the case for ^{20}Ne), this assumption is not valid so optical model parameters specific for these nuclei have to be determined [Bar67].

2.2.3 Spectroscopic Factors

In equation 2.24, the term $(\psi_\beta|W|\psi_\alpha)$ contains the nuclear structure information. The present discussion will be restricted to the specific case of transfer reactions. Therefore, this term can be rewritten as $(\psi_a\psi_A|W|\psi_b\psi_B)$. Consider the case of one nucleon transfer and the decomposition $B \to A + x$ (and $b \to a + x$). It is convenient to introduce the internal coordinates for nucleus i, ζ_i. The residual interaction in the post form can then be written as

$$W_\beta \equiv V_{bB} - U_\beta = V_{xA}(\mathbf{r}_{xA}, \zeta_x, \zeta_A) + V_{bA}(\mathbf{r}_{bA}, \zeta_b, \zeta_A) - U_\beta(\mathbf{r}_\beta, \zeta_b, \zeta_B). \quad (2.27)$$

The different terms in this expression might excite their corresponding nuclei, but typically these excitations can be neglected. If internal excitations are neglected,

then W commutes with ψ_A and ψ_a Then $(\psi_a\psi_A|W|\psi_b\psi_B)$ reduces to the product of W and the overlap functions (ψ_B, ψ_A) and (ψ_b, ψ_a). The overlap functions $\phi_i^j = (\psi_i, \psi_j)$ represent the projections of the state i onto the state j. Now it is useful to define a spectroscopic factor, $S_{\ell j}$, as the norm of the square of the overlap function,

$$S_{\ell j}(A, x|B) = \int |\phi^B_{A\ell j}|^2 d\mathbf{r}_{xA} d\zeta \tag{2.28}$$

The spectroscopic factor can be interpreted as the probability that the state B is a composition of state A plus the nucleon x, each with their corresponding angular momenta. In other words, it tells how the state B acts like an inert core with the valence nucleon x determining the properties of the nucleus. If ϕ is decomposed into its radial $(R^B_{Alj}(r_{xA}))$ and angular components, then the equation for the spectroscopic factor can be integrated over ζ and the angular components. This leaves,

$$S_{\ell j}(A, x|B) = \int |R^B_{A\ell j}(r_{xA})|^2 r^2_{xA} dr_{xA}. \tag{2.29}$$

Sometimes the isospin Clebsch-Gordon coefficient is combined with the spectroscopic factor as the product C^2S. Looking at equations 2.24 and 2.28, it is clear that the transition element is also proportional to the overlap functions. The cross section is proportional to the square of the DWBA transition amplitude. This in turn is proportional to the overlap functions, the squared-norm of which define spectroscopic factors. Therefore, it can be shown that

$$\frac{d\sigma}{d\Omega}^{exp} \propto \sum_{\ell_A \ell_B j_A j_B} S_{\ell_B j_B}(A, x|B) S_{\ell_a j_A}(b, x|a) \sigma^{DW}_{\ell_B j_B \ell_A j_A} \tag{2.30}$$

The shape of the distribution is very sensitive to the orbital angular momentum ℓ of the transferred nucleon.

Extracting spectroscopic factors from data traditionally is done using a ratio of cross sections

$$\frac{d\sigma^{exp}}{d\Omega} = S^{exp}\frac{2J_b+1}{2J_B+1}\frac{d\sigma^{DWBA}}{d\Omega} \tag{2.31}$$

Spectroscopic factors determined from an experiment are model dependent. Spectroscopic factors depend upon the optical model parameters used in the DWBA calculations [Nun09].

Many codes exists to perform transfer reaction calculations. The present study utilized TWOFNR to interpret the data [Igar]. TWOFNR is a DWBA code written in FORTRAN that uses the Woods-Saxon form for the optical model potential. This code allows the user to either input their own optical model parameters or use a global set, such as Perey [Per76]. For the ^{15}N(d,p) measurement the global parameters of Perey were well suited for the DWBA calculations.

2.3 R-matrix Theory

DWBA theory assumes that the reaction is direct, i.e. the reaction progresses directly from state α to state β. In many circumstances, however, there is an intermediate state populated called a compound nucleus and a different method of describing the reaction is needed. Discrete states exist in the compound nucleus, and as such the cross section is enhanced when the energy of the initial system matches that of the physical state. The energy at which this enhancement occurs is the resonance energy and corresponds to the energy of the compound nuclear state. These resonances have a particular strength and width that are physical quantities, regardless of what formalism is used to describe them. The parameters $\gamma_{\lambda c}$ are called the *reduced widths* and the *observed width* (Γ) can be expressed in terms of these using the relation

$$\Gamma_{\lambda c}(E) = 2P_c(E)\frac{\gamma_{\lambda c}^2}{(1+\gamma_{\lambda c}^2 S'(E_R))}. \tag{2.32}$$

where $S'(E)$ is the is the Coulomb shift function defined in Lane and Thomas [Lan58].

Therefore, the final cross section can be described in terms of an observed experimental width and the internal eigenstate which depends on the channel radius and boundary conditions. When the width of the resonance is much smaller than the level spacing [Bet37], the cross section can be expressed as

$$\sigma_{\alpha\alpha'} = \frac{\pi}{k_\alpha^2}\sum_{Jsls'l'} g_J \left| \sum_\lambda \frac{\Gamma_{\lambda c}^{1/2}\Gamma_{\lambda c'}^{1/2}}{E_\lambda + \Delta_\lambda - E - \frac{i}{2}\Gamma_\lambda} \right|^2 . \tag{2.33}$$

R-matrix theory is a powerful tool of quantum physics whose main aim is to describe scattering states resulting from the interaction of nuclei. It involves parameterizing space into two regions: the internal region and the external region. The boundary between these two is defined by a parameter called the channel radius, a_c. It is defined in such a way that the only forces acting in the external region are long range forces, such as the electromagnetic interaction. On the other hand, the internal region contains the short-range nuclear interactions. The scattering wave function is approximated by its asymptotic form. Since the internal region is confined, its eigenstates form a discrete basis and the scattering wave function is expanded over these eigenstates. The R-matrix is the part of the expansion of the collision matrix that accounts for all the interactions within the nucleus and is the inverse of the logarithmic derivative of the wave function at the boundary.

Certain assumptions are at the core of R-matrix theory. *(i)* Non-relativistic quantum mechanics must be applicable to the reaction, though this is common among many theories in low energy nuclear physics. This assumption is justified

by the fact that kinetic energies inside nuclei are much smaller than the rest energy of the nucleons. *(ii)* The processes involved in this measurement do not lead to the production of more than two nuclei. Therefore it would not be readily applicable to a reaction in which three-body forces are important. *(iii)* There are no important processes involved that lead to the creation or destruction of particles, though the main effect of this assumption is to exclude photons. The following discussion is adapted from [Lan58, Rui03, Bet37].

As with most theories, the R-matrix aims to solve the radial Schrödinger equation, both in the internal and external regions.

$$-\frac{\hbar^2}{2m}\frac{d^2\psi}{dr^2} + V(r) = E\psi \tag{2.34}$$

To represent the wavefunction, a set of stationary states are used:

$$\Psi = \sum_{\lambda} A_\lambda \mathrm{X}_\lambda \tag{2.35}$$

where the coefficients A_λ are of the form

$$A_\lambda = \int_V \mathrm{X}_\lambda \Psi dV \tag{2.36}$$

These stationary states satisfy the Hamiltonian $H\mathrm{X}_\lambda = E_\lambda \mathrm{X}_\lambda$, where X_λ are the eigenvectors of corresponding eigenvalues E_λ. To make sure that these states relate directly to the actual *quasi-bound* states at the nuclear surface $r = a_c$, a boundary constant, b, is introduced which gives the boundary condition

$$\frac{d\mathrm{X}_\lambda}{dr} + b\mathrm{X}_\lambda|_{r=a_c} = 0 \tag{2.37}$$

By substitution and integration the following is obtained:

$$-\frac{\hbar^2}{2m}\left(\Psi\frac{dX_\lambda}{dr} + X_\lambda\frac{d\Psi}{dr}\right)_{r=a_c} = (E - E_\lambda)\int_0^{a_c} X_\lambda \Psi dr \tag{2.38}$$

which then, using the earlier definition of A_λ, leads to

$$A_\lambda = -\frac{\hbar^2}{2m} X_\lambda(a_c) \frac{\Psi'(a_c) + b\Psi(a_c)}{E - E_\lambda} \tag{2.39}$$

Now the $\Psi(r)$ can be written as

$$\Psi(r) = G(r, a_c)(\Psi'(a_c) + b\Psi(a_c)) \tag{2.40}$$

where $G(r, a_c)$ is the Green's function and is given by:

$$G(r, a_c) = -\frac{\hbar^2}{2m} \sum_\lambda \frac{X_\lambda(r) X_\lambda(a_c)}{E_\lambda - E}. \tag{2.41}$$

The *R-function* is defined as the value of the Green's function at $r = a_c$.

$$R \equiv G(a, a) = -\frac{\hbar^2}{2m} \sum_\lambda \frac{X_\lambda^2(a_c)}{E_\lambda - E} \tag{2.42}$$

To simplify the expression, a new parameter is introduced, γ_λ, such that $\gamma_\lambda^2 = \frac{\hbar^2}{2m}|X_\lambda|^2$. The R-function then becomes

$$R = \sum_\lambda \frac{\gamma_\lambda^2}{E - E_\lambda} \tag{2.43}$$

The R-function provides a convenient way to express the logarithmic derivative of the wave function at the nuclear surface, which will be useful later.

$$\frac{\Psi'(a)}{\Psi(a)} = \frac{(1 - bR)}{R} \tag{2.44}$$

The total wave function in the external region can be written as the superposition of the incoming (I) and outgoing waves (O):

$$\Psi_\ell = I_\ell - U_\ell O_\ell \tag{2.45}$$

where the index ℓ denotes the incident orbital angular momentum of the system and U_ℓ is the *collision function*. It is useful to consider U_ℓ as the amplitude of the unit-flux outgoing wave O_ℓ, which is associated with a unit-flux incoming wave I_ℓ. The incident and outgoing waves can be expressed in terms of the

regular and irregular Coulomb functions F_ℓ and G_ℓ and the Coulomb phase shift $w_\ell = \sum_{n=1}^{\ell} tan^{-1}(\frac{n_\ell}{n})$ by

$$I_\ell = (G_\ell - iF_\ell)e^{iw_\ell} \tag{2.46}$$

$$O_\ell = (G_\ell + iF_\ell)e^{-iw_\ell} \tag{2.47}$$

Now we are able to construct the *nuclear scattering amplitude* A as well as the differential cross section $\frac{d\sigma}{d\Omega}$:

$$A(\theta) = \frac{1}{2}ik^{-1}\left|\sum_\ell (2\ell+1)(1-U_\ell)P_l(cos\theta)\right|^2 \tag{2.48}$$

$$\frac{d\sigma(\theta)}{d\Omega} = |A(\theta)|^2 = \frac{1}{4}k^{-2}\left|\sum_\ell (2\ell+1)(1-U_\ell)P_\ell(cos\theta)\right|^2 \tag{2.49}$$

where P_ℓ represent the standard Legendre polynomials.

We can express the collision function U_ℓ in terms of the R-function by utilizing the boundary conditions and equating the logarithmic derivatives of the internal and external wave functions at the nuclear surface ($r = a_c$). Then U_ℓ can be expressed in terms of a phase shift, δ_e

:

$$U_\ell = e^{2i\delta_\ell} \tag{2.50}$$

where

$$\delta_\ell = tan^{-1}\left(\frac{p_\ell R_\ell}{1 - R_\ell S_\ell}\right) - \phi_\ell \tag{2.51}$$

Here ϕ_ℓ, p_ℓ, and S_ℓ are the hard-sphere phase shift, penetrability, and energy shift function, respectively and can be found in [Lan58].

In many cases there are usually multiple states and channels open and multiple combinations of spin that contribute to the formation of states of different spin-parity. The collision function and R-function then become the collision matrix and R-matrix with indices $c = [\alpha s \nu \ell m]$ which represent the channel, channel spin, channel spin component, orbital angular momentum, and orbital angular momentum component. The derivation for cross section for this more complicated case is similar so here the results will be summarized. A more complete derivation can be found in [Lan58].

$$R_{cc'} = \sum_{\lambda} \frac{\gamma_{\lambda c}\gamma_{\lambda c'}}{E_\lambda - E} \tag{2.52}$$

$$U_{cc'} = \left(\frac{k_c r_c}{k_{c'} r_{c'}}\right)^{1/2} \frac{(1 - RL_c^*)I_{c'}}{O_c(1 - RL_)} \tag{2.53}$$

with $L_c \equiv S_c - B_c + iP_c$, with B_c being the matrix form of the boundary constant.

Chapter 3
Experimental Tools

Nuclear physics is largely the study of nuclear interactions. This means that for a given reaction, scientists need to both understand the properties of the particles going into the reaction and of those that come out. Typically there is a great deal of control over what goes into the reaction, but detecting the outgoing particles can be trickier. Experimentalists have many tools at their disposal to detect the particles of interest. However, it may first make sense to begin with the production of the beams themselves. In this chapter I will first describe how the beams are created for the experiment. Next I will describe the various detectors used for the measurements of this dissertation, as well as describe how these types of detectors function.

3.1 Beam Production

One of the most important aspects of an experiment is the creation of the beam, without which the measurement is not possible. The beams for each of these measurements were created using the cesium ion source at the Holifield Radioactive Ion Beam Facility (HRIBF) at Oak Ridge National Laboratory (ORNL). Figure 3.1 shows a schematic of how the source works. Cesium is heated in an oven to create cesium vapor which fills an enclosed area between the cooled cathode and the heated ionizing surface of the source material. The cesium can condense on the front of the cathode or become ionized by the hot surface. This ionized cesium

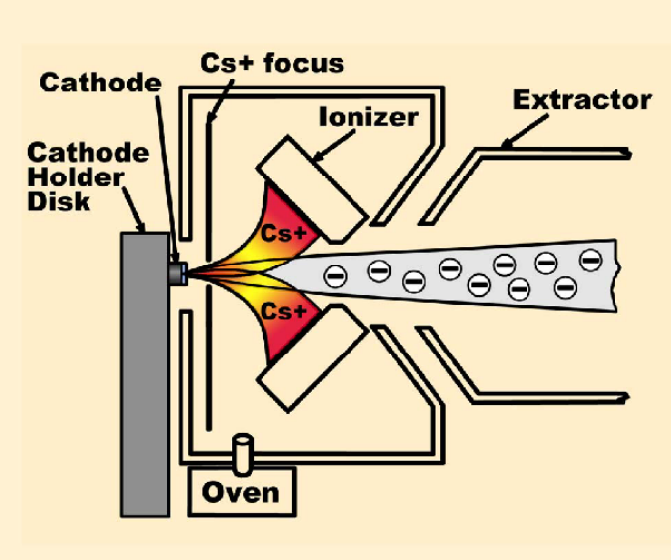

Figure 3.1: A schematic demonstrating how a cesium ion source works.

accelerates towards the cathode, sputtering particles from the cathode through the condensed cesium layer. After passing through the cesium, these particles are negatively charged. These negative ions are then injected into the 25-MV tandem accelerator.

The negatively charged ions are accelerated up the tandem to the positively charged terminal. At the top the beam passes through a carbon foil which strips several electrons, leaving the ion positively charged. The beam is then accelerated down the high-energy side of the tandem to reach its full energy. If particularly high energies are needed, it is possible to strip the ions again with another foil placed about a third of the way down the tandem. This increases the net charge of the ion and thus increases the force it feels, allowing higher energies to be achieved. Once the beam reaches full energy, it is delivered to the target station.

3.2 Detectors

When detecting particles, the important quantities to measure are the angles at which a given particle left the nucleus, its energy, atomic number, and mass. These values enable the experimentalist to determine what reaction occurred and where all of the energy and momentum in the reaction went. Determining the angle is relatively simple since all that is required is to set the detector(s) at the angle(s) you wish to cover. To determine the energy, you need to ensure that the response of the detector is proportional to the energy deposited. Determining the mass and atomic number (i.e. particle identification) can be accomplished through a variety of ways. Multiple detectors could be placed in the particle's path. Since the amount of energy a particle loses as it travels through matter is a function of its mass and atomic number as well as its energy, comparing the energy deposited in each layer to the total energy is one way of separating different species. The types of detectors and techniques used are determined by the requirements of the measurement.

3.2.1 Semiconductor Detectors

Silicon semiconductors are crystalline materials whose outer shell atomic levels exhibit an energy band structure. This band structure consists of a valence band in which the electrons are confined to their atoms, a conduction band in which the electrons are free to move along the crystalline structure, and an energy gap in between. The reason that semiconductors make better detectors than many other materials is that at room temperature thermal energies would not be enough to excite many of the electrons from the valence band into the conduction band. However, relatively low energy particles (such as 200 keV protons) interacting with the material could induce a measurable current. As the electrons get excited, a

hole is created in the valence band which acts as a positive charge carrier. The measured current is actually a product of both sources: the movement of free electrons in the conduction band and the movement of holes in the valence band.

Often semiconductors are *doped* with impurities that bring extra electrons that are free to roam about the conduction band (n-type) or with extra"holes" that are free to roam about the valence band (p-type). All present day semiconductor detectors depend on the formation of a *junction*, formed by the juxtaposition of a p-type semiconductor and an n-type semiconductor. The free electrons from the n-type material drift across the gap to fill in the holes in the p-type material, creating a net negative charge in the p-type material and leaving a net positive charge in the n-type material. This separation of charges creates an electric field which sweeps out the electron-hole pairs created by radiation entering the detector. Generally this volume is confined near the junction, but by applying a *reverse bias* (negative voltage to the p-side and positive voltage to the n-side) the effective volume of this zone can be enhanced. Contacts on either end of the junction device will allow the current to be measured, giving information about the energy deposited by the particle. In these measurements a variety of silicon detectors were used and will be discussed below.

SIDAR

For both the ^{20}Ne(p,d) and the ^{15}N(d,p) experiments, the SIlicon Detector ARray SIDAR was used to detect the outgoing particles [Bar99]. SIDAR consists of Micron Semiconductor YY1 wedges with 16 0.5-cm annular strips per wedge that have an inner radius of 5 cm and an outer radius of 13 cm. This array can either be mounted flat, in which case 8 wedges are required to complete the array, or in a lampshade geometry, requiring only 6 wedges (see Figure 3.2). Both configurations have their advantages. In its lampshade mode, SIDAR is tilted

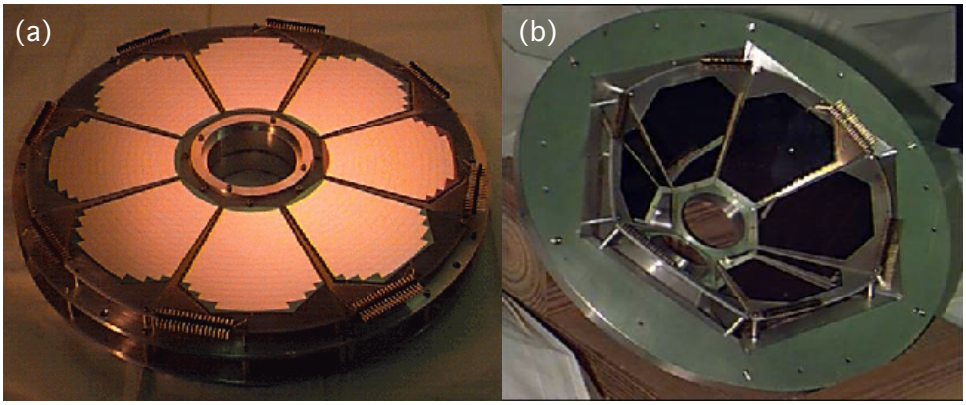

Figure 3.2: **(a)** The SIDAR silicon detector array in its flat mode, consisting of 8 YY1 detectors. **(b)** The SIDAR silicon detector array in its lampshade configuration, consisting of 6 YY1 detectors. [Bar11]

towards the target so it covers a larger solid angle. However, doing so results in each strip having a larger angular width which corresponds to a lower energy resolution [Bar99].

MINI

MINI was implemented in the ^{7}Be+d measurement to detect the elastically scattered deuterons. It is an S1-style 300-micron thick silicon detector also from Micron Semiconductor. MINI is a smaller annular detector consisting of 4 quadrants of 16 1.5-mm strips with an inner radius 2.4 cm and an our radius of 4.8 cm (see Figure 3.3). In practice, MINI has an intrinsic energy resolution of ≈ 60 keV for a 5.8 MeV alpha particle.

ORRUBA

In recent years, a new detector array has been developed, called the Oak Ridge Rutgers University Barrel Array (ORRUBA), shown in Figure 3.4 [Pai07]. The motivation for its development came from a growing interest in experiments with

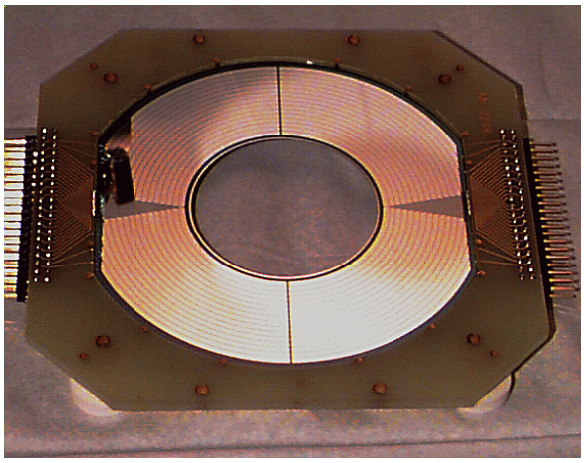

Figure 3.3: The MINI detector, an S1-style silicon detector developed by Micron Semiconductor. [Bar11]

beams of unstable nuclei. Due to their short half-lives, doing experiments the traditional way with heavy targets is difficult. However, in inverse kinematics (heavy beam on a light target) the reaction can occur before the heavy nuclei in the beam decay. In these cases the center of mass frame and the laboratory frame are no longer approximately the same, as is the usual case for low energy nuclear experiments with light beams on heavy targets.

Transfer reactions with low angular momentum transfer tend to be sharply peaked at forward center of mass angles, which corresponds to backward laboratory angles. However, the (d, p) angular distributions in the laboratory frame are shaped differently. As is evident in Figure 3.5, the angular distributions are spread over a larger angular range and are now peaked at more forward laboratory angles, near $\theta_{lab} = 120°$. With the relatively low beam intensities available for radioactive ion beams, it is important to cover as much of the solid angle as possible. For this reason ORRUBA was developed since detectors like MINI and SIDAR are not suited for covering this angular region.

ORRUBA consists of two rings of silicon detectors. The full array covers

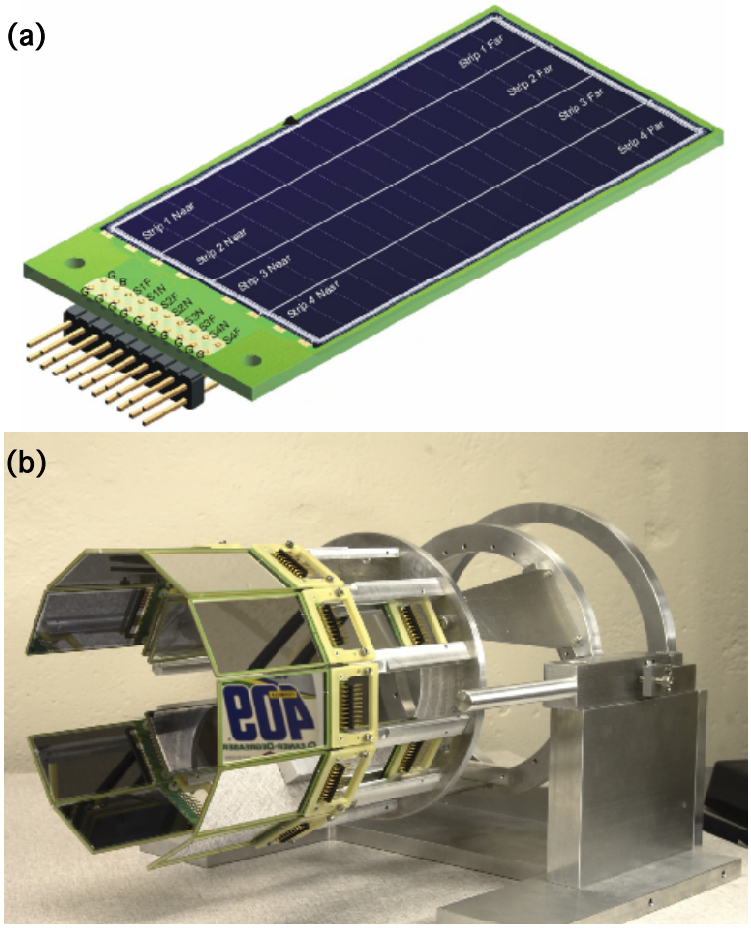

Figure 3.4: **(a)** A diagram of one of the ORRUBA detectors. It is a silicon detector comprised of 4 resistive strips, each 7.5 cm long and 1 cm wide. **(b)** Fully assembled ORRUBA covering 80% of the azimuthal angular range. [Pai11]

$\theta_{lab} = 45° - 135°$ and about 80% of the azimuthal angle. Each ORRUBA detector is comprised of 4 resistive strips of silicon, with an active area 7.5 cm long and 1 cm wide. When a charged particle interacts with a strip, the induced charge is read out on each end of the strip. Since the resistance is constant per unit length for these strips, the difference in the charge measured by each end can be used to determine the position of the interaction. In practice the position resolution is a function of energy, but generally it is < 2 mm. Figure 3.6 shows a plot of position resolution as a function of energy deposited in ORRUBA. These data

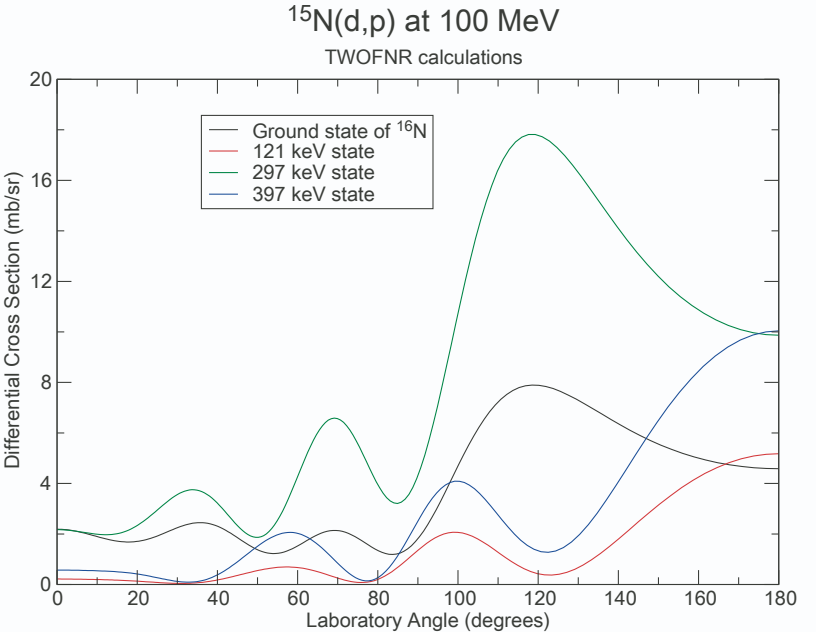

Figure 3.5: TWOFNR calculations of differential cross sections as a function of laboratory angle for the ^{15}N(d,p) reaction with $E_{^{15}N} = 100$ MeV. Note how the differential cross sections peak around $\theta_{lab} = 120°$. The different curves correspond to different excited states in ^{16}N.

were primarily taken from elastic scattering of protons from a gold target. The two curves represent a different offset-resister placed between the strip and the preamplifier. The important thing to note though is the overall dependence of position resolution on energy. The point at 5.8 MeV was acquired using an alpha source. In an ideal situation, ORRUBA's intrinsic energy resolution is around 60 keV, as with MINI. In practice however, ORRUBA typically achieves an energy resolution of ≈ 100 keV.

Due to the fact that the strips are resistive, the position of the particle interacting with the detector can be determined. When a particle deposits energy in an ORRUBA strip, the signal is read out at both ends of the strip. The way in which the signal splits between ends depends on the resistance between where the event occurred and each end. Since the resistance per unit length of each strip

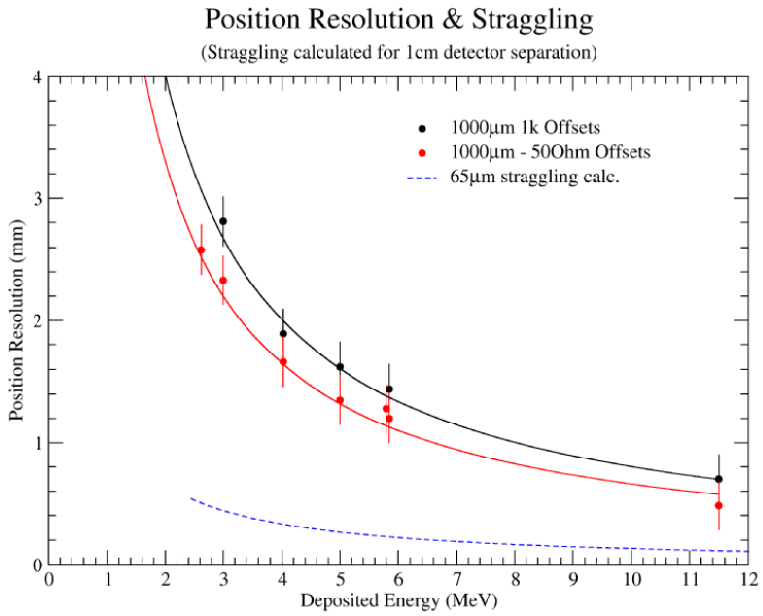

Figure 3.6: Position resolution of ORRUBA as a function of the energy deposited. These data are for protons elastically scattered from a gold target. The point at 5.8 MeV was obtained using an alpha source. See text for more details.

is constant, the further away the event occurred from an end the more resistance it "sees" to that end. In this way, the closer end will see a stronger signal than a further one. The stronger end is called *hi* and the lower end is called *lo*. Note that we know which end corresponds to the *hi* signal. The position is calculated using:

$$pos = \frac{hi - lo}{hi + lo} \tag{3.1}$$

If *pos* is close to 0, then the event occurred near the center of the strip. If *pos* is close to 1, then the event occurred near the hi end of the strip. As is clear by this equation, $0 \leq pos \leq 1$, where *pos* is then calibrated to represent the length of the strip (75 mm) using an alpha source which should illuminate the entire strip. The length of the alpha line in the Energy vs Position plots (see Figure 3.7) represents the length of the strip. The position is then converted into θ_{lab}.

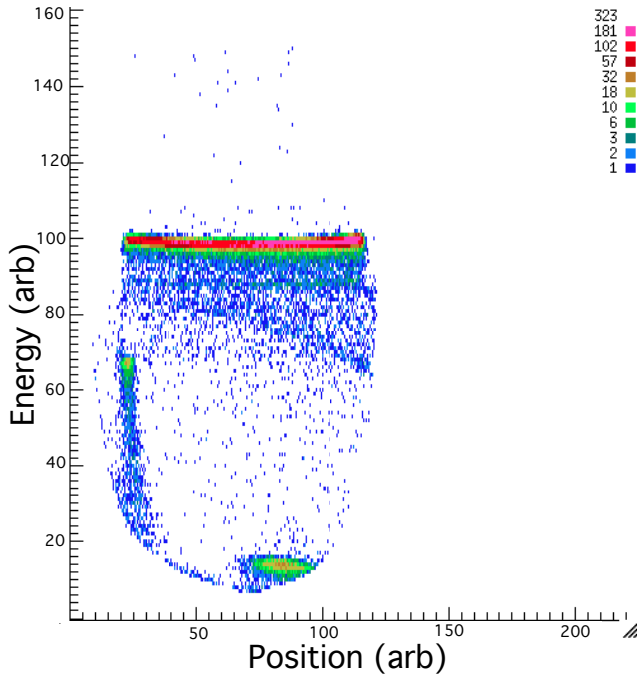

Figure 3.7: The energy measured by one ORRUBA strip plotted against the position for the 5.8 MeV alpha source.

3.2.2 Ionization Chamber

Often, especially when doing experiments in inverse kinematics with heavy beams, the beam is contaminated by an isotope with the same mass and charge. In principle, all species in a "cocktail" beam can interact with the target and produce the same outgoing particles. It is important to be able to separate the events that were induced by each beam species. The best way to do this in most cases is to detect the heavy recoils from the target and separate the species. In the case of the ^{7}Be+d study, this separation was accomplished by the use of an ionization chamber.

A segmented, gas-filled ionization chamber was used where the energy deposited by the particle leads to ionization of the gas within. Electrodes parallel to the particle's path collect the ionization charges. By applying an external electric

field across the electrodes, the ionized electrons are swept towards the segmented anodes. The remaining ions in the gas are swept towards the cathode. The pressure of the gas is set high enough that the beam-like recoils are stopped within the detector volume, but low enough that the particles completely pass through the first anode. The gas chosen for the ionization chamber was tetrafluromethane (CF_4) since the drift velocity of electrons in this gas is relatively fast. Faster drift velocities mean that the ionization chamber can handle a higher beam intensity. Currently this chamber can handle beams with currents $< 1 \times 10^5$ particles per second.

The ionization chamber is able to separate the different nuclei in the beam is because the stopping power of the gas is strongly dependent on the beam species. The famous Bethe-Bloch formula shows the dependence of the stopping power on the atomic number(z) and mass (m_0) of the beam:

$$-\frac{dE}{dx} = \frac{4\pi e^4 z^2}{m_0 v^2} N_a Z \left[\ln\left(\frac{2\gamma^2 m_0 v^2}{I} \right) - \beta^2 \right] \tag{3.2}$$

where v is the velocity of the incident particle, N_a is Avogadro's number, Z is the atomic number of the absorbing material, I is the mean excitation potential, and $\beta = v/c$ [Leo87].

All of the energy is not deposited in the first anode of the ionization chamber. Equation 3.2 shows that particles with the same energy but different nuclear charge, as in the case of the beam contaminants in these experiments, will deposit different amounts of energy in the first region. So particle identification can be achieved by comparing the energy lost in the anode region to the total energy of the particle. Figure 3.8 shows an example of this separation achieved in the ^{7}Be+d experiment. In the case of the ^{7}Be beam, the ionization chamber was used to monitor the intensity of the beam current as well as verify beam purity.

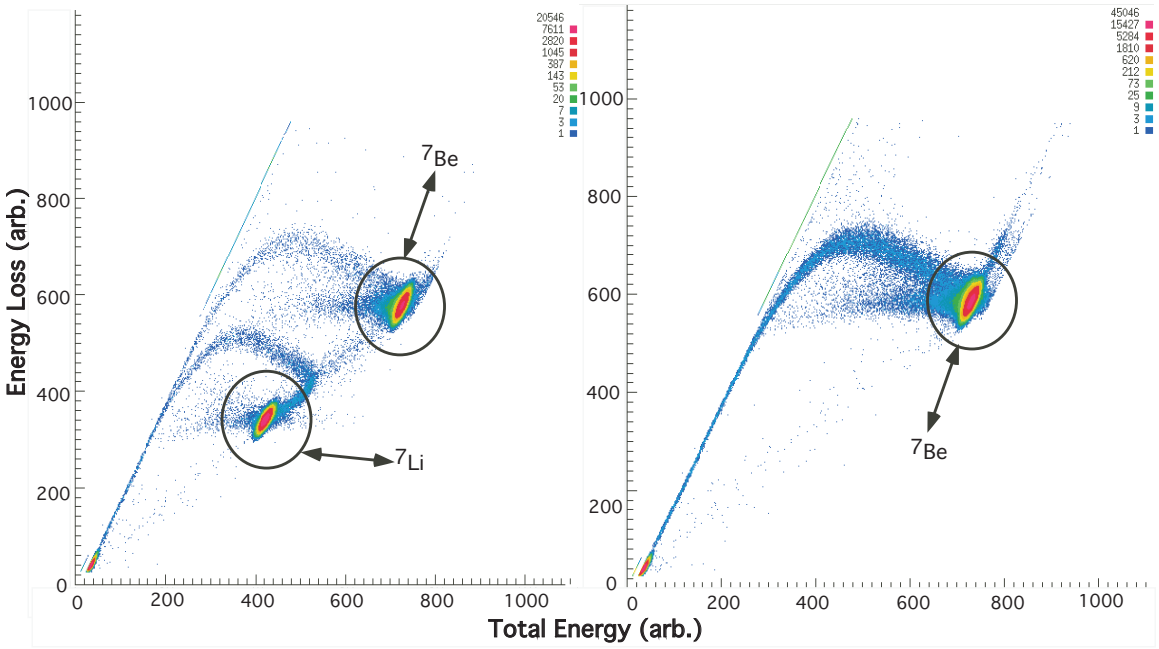

Figure 3.8: **(a)** Ion counter spectrum of energy loss as a function of total energy of the A=7 beam stripped to charge state 1^+. Note the presence of the ^{7}Li contamination. **(b)** Ion counter spectrum of beam stripped to charge state 4^+, indicating a pure ^{7}Be beam.

3.3 Electronics

Each of these detectors output a current signal that is proportional to the energy and needs to be recorded. For each of the measurements discussed in this dissertation, the pulse-shaping and digitizing electronics used to store the detector pulse heights were nearly identical. For the sake of brevity let us focus on the ^{7}Be+d study. Figure 3.9 shows a schematic of the electronics used in this measurement. Rather than cover every detail, a few of the important points to note will be covered.

The trigger for the data acquisition was a combination of logic signals from a hit in the silicon detectors (MINI in this case). The ionization chamber can handle event rates of up to 10^5 events per second, but the acquisition system

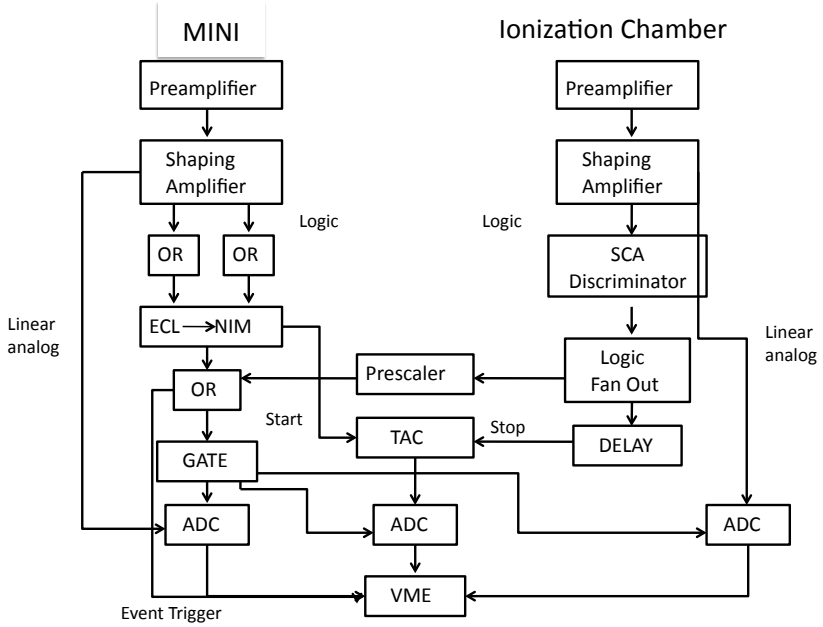

Figure 3.9: A schematic of the electronics used for the ^{7}Be+d measurement.

can not. When including the ionization chamber in the trigger, it was necessary to implement a prescaler that outputs a logic pulse for every 2^9 events in the ionization chamber. The detector signals themselves were amplified in shaping amplifiers and then put through an analog-to-digital converter (ADC) to transform the signal pulse height into a form that the data acquisition (VME) can interpret.

Chapter 4

Search for a resonant enhancement of the ^{7}Be+d reaction and primordial ^{7}Li abundances

4.1 Introduction

Big Bang Nucleosynthesis (BBN) models used to calculate the abundance of light elements produced in the Big Bang are functions of many parameters. One of the most important parameters for these calculations is the baryon density which was recently determined with great precision by WMAP. It is often expressed as the baryon to photon ratio ($\eta = 6.2 \pm 0.2 \times 10^{-10}$) [Spe03].

In order to refine this theoretical model, comparisons must be made to early universe abundances. This is done using observations of low metallicity stars. Low metallicity stars are stars with small amounts of elements heavier than helium. Most of the elements heavier than helium were produced in stars after the big bang. So low metallicity stars are likely older stars formed from gases representative of the post big bang universe. In the case of lithium, by looking for a characteristic atomic lithium line at 670.7 nm, its abundance in these stars can be measured (see Figure 4.1) [Smi98]. These data are fit as a function of metallicity and extrapolated to 0 to represent the primordial abundance, commonly accepted as $^7\mathrm{Li/H} = 1.23^{+0.34}_{-0.16} \times 10^{-10}$ [Rya00].

Estimates of abundances of several light nuclei are shown in Figure 4.2. The curves represent the calculated isotopic abundance from BBN theory as a function of the baryonic density. The horizontal shaded areas represent the values

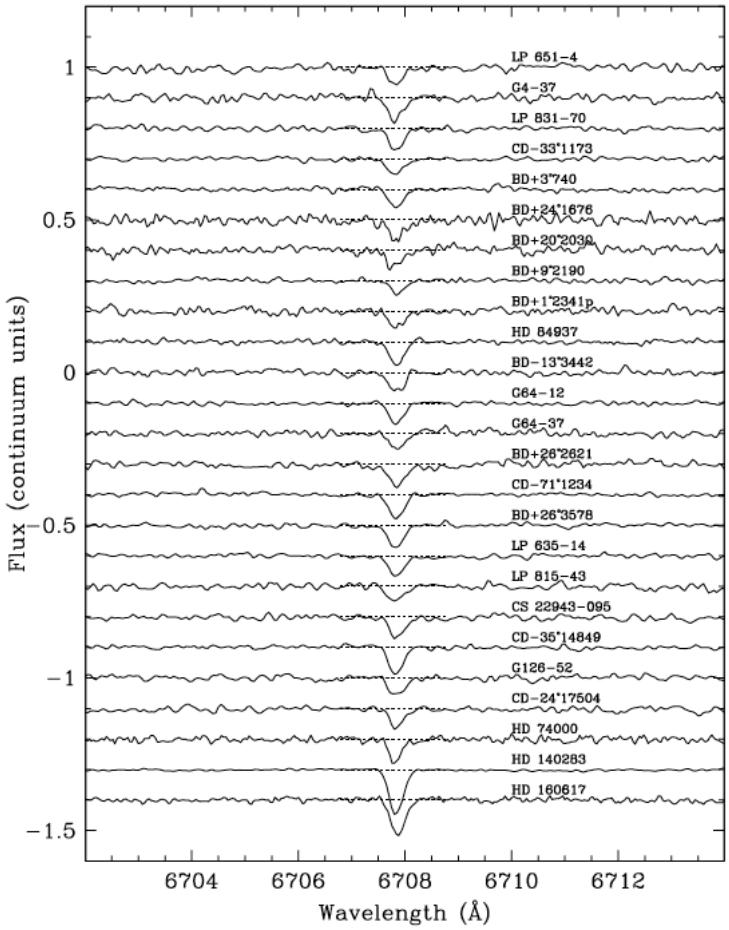

Figure 4.1: A portion of the light spectrum from several low metallicity stars that displays the flux as function of wavelength. The characteristic lithium line is at 6707 angstroms. This figure is adopted from [Rya99].

as extrapolated from measurements of low metallicity stars. The vertical shaded areas represent WMAP's determination of the baryonic density. With WMAP's value for the baryonic density, the densities of D and ^{4}He are in reasonable agreement with the values predicted by BBN theory. However, in the case of ^{7}Li there is considerable discrepancy (observed abundance is almost a factor of 4 smaller than that predicted by BBN models). The high precision measurement of this cosmological parameter has led to much higher precision in BBN calculations. In particular, the abundance of ^{7}Li after the period of BBN was predicted to be

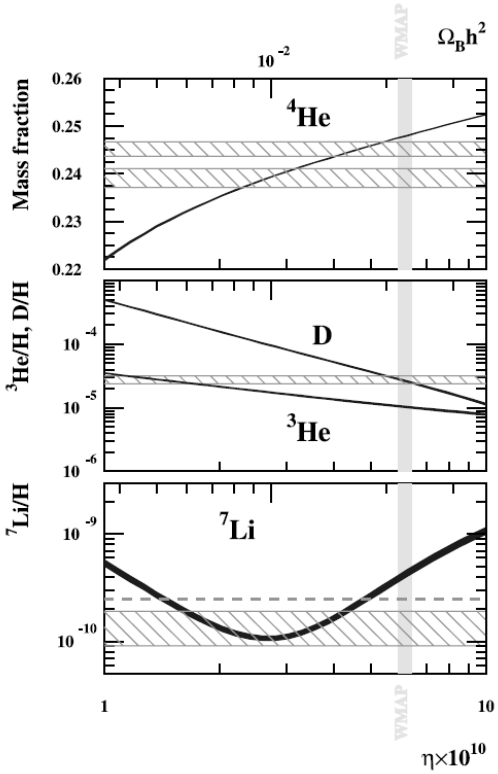

Figure 4.2: Calculated BBN abundance relative to hydrogen for several light isotopes as a function of the baryonic density. The curves represent theoretical predictions as a function of the baryonic density ($\Omega_b h^2$) and the baryon to photon ratio (η). The vertical shaded bar shows WMAP's recent determination of the baryonic density and the horizontal shaded regions represent abundances extrapolated from observations. Note that for the case of ^{4}He, the two horizontal shaded regions represent competing observations for its abundance [Coc04].

$^7\mathrm{Li/H} = 5.12^{+0.71}_{-0.62} \times 10^{-10}$, almost a factor of 4 larger than values extrapolated from observations [Cyb08].

Several solutions have been proposed to resolve this discrepancy. A possible astrophysical solution is that the current understanding of the stellar processes that deplete lithium in population II stars needs to be improved [Ric05]. Another possibility is that physics beyond the standard BBN model is required, such as a variation in the strong force during the first few seconds of the Big Bang [Pos11]. Another solution that has been proposed is the existence of a negatively charged

massive unstable particle, X^-. These particles are thought to decay into the present dark matter and could act as a catalyst for the destruction of ^{7}Be (which decays into ^{7}Li) and ^{7}Li.

A proposed nuclear physics resolution could be a resonant enhancement of the destruction of ^{7}Be in the early universe higher than was previously considered. Which results in less ^{7}Be being available to decay to ^{7}Li, reducing the predicted BBN abundance [Coc04] which was a factor of ≈ 4 larger than values extrapolated from observation. Recent work by [Cyb09] predicted that if a $5/2^+ \sim 16.7$-MeV state in ^{9}B has a ^{7}Be+d resonance energy between 170-220 keV and a deuteron decay width between 10-40 keV, then a resonant enhancement of the $^7\mathrm{Be}(d,p)2\alpha$ or $^7\mathrm{Be}(d,\gamma)$ reaction could resolve the cosmological lithium problem.

There has been a recent measurement of the $^7\mathrm{Be}(d,p)2\alpha$ reaction. This measurement by was done by [Ang05] and no enhancement of the rate was found when compared to prior calculations and early work by [Kav60]. However, [Cyb09] argue that some of the assumptions made in this earlier measurement may not be valid. Furthermore, (d,p) protons populating the 16.63-MeV 2^+ state in ^{8}Be would have been missed in that study, since they were below the detection threshold. In more recent work, [Boy10] question whether the resonance would be populated in the ^{7}Be+d reaction. Clearly more study of possible resonances in $^7\mathrm{Be}+d$ reactions and the 16.7-MeV state in ^{9}B is needed to resolve these issues.

4.2 Experiment

The $d(^7\mathrm{Be},d)^7\mathrm{Be}$ reaction was used to search for the predicted resonance at the Holifield Radioactive Ion Beam Facility (HRIBF) at Oak Ridge National Laboratory (ORNL) [Bee11]. The experiment was performed in inverse kinematics using a pure 10-MeV ^{7}Be beam with an average intensity of 5×10^4 ^{7}Be/s. The ^{7}Be

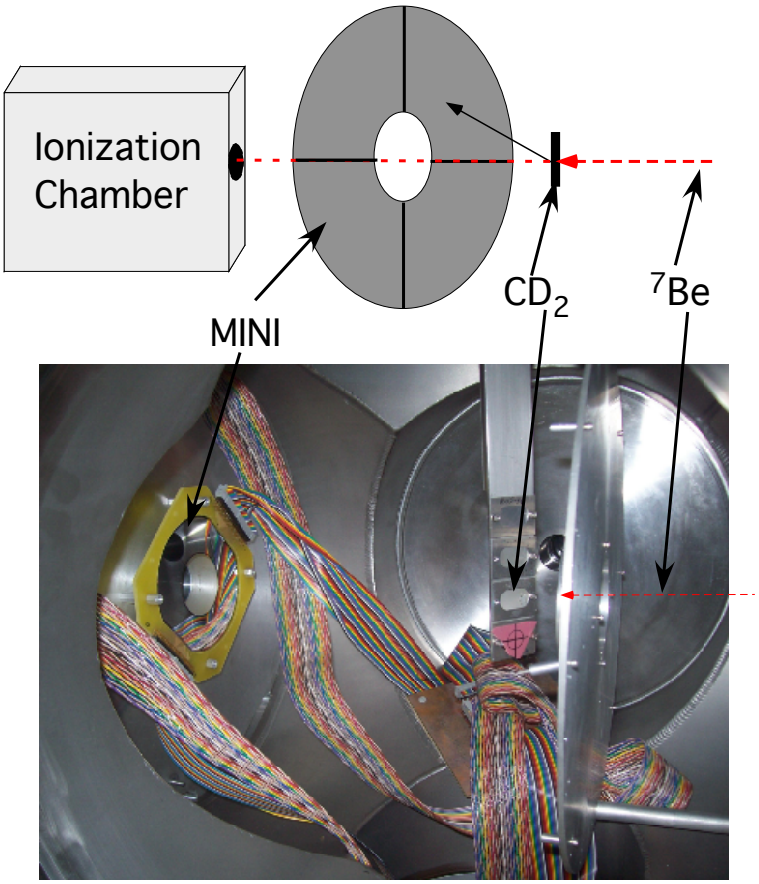

Figure 4.3: The experimental setup for the $d(^7\mathrm{Be}, d)$ measurement. The top figure is a schematic of the setup shown in the photograph below it. The beam enters from the right and the ion chamber was placed downstream past the MINI detector to the left. Multiple CD_2 targets were mounted on the target ladder.

was produced at the Institute of Nuclear Research of the Hungarian Academy of Sciences (ATOMKI) via the $^7\mathrm{Li}(p, n)^7\mathrm{Be}$ reaction and shipped to ORNL, where it was chemically isolated from the ^{7}Li and pressed into a cathode for use in a sputter ion source. These cathodes were then placed in a multi-sample, Cs-sputter ion source that was mounted on the IRIS1 radioactive-ion beam production platform.

This ion source produces negative ions by a process of cesium sputtering on the surface of the cathode. This sputtering results in negative ions being ejected from the surface of the cathode and extracted from the ion source to form a beam.

It is the same type of ion source that is used for the stable beam injector to the Tandem Electrostatic accelerator. One significant difference is that the stable-beam source for the Tandem holds a single cathode, while the radioactive ion source can hold up to 4 cathodes that can be changed without breaking vacuum. This capacity allows the loading of the target wheel with more than one cathode containing beryllium and other cathodes to be used for tuning (e.g. a lithium cathode for tuning ^{7}Li as a pilot beam). Beryllium does not form negative ions very efficiently, so a mixture of ^{7}Li and ^{7}Be is extracted from the ion source as negatively charged molecules of beryllium oxide (BeO) and lithium oxide (LiO). At the terminal, the oxide molecules are broken up at the carbon stripper foil and the resultant ^{7}Be ions accelerated to full energy of 10 MeV. In some cases, there is still a measurable number of lithium ions in the beam, but these can be removed by fully stripping the ions as the beam exits the Tandem and selecting only the q=4^{+} ions.

The 10-MeV ^{7}Be beam was used to bombard a 1.62-mg/cm^{2} thick CD_2 target. Scattered deuterons from the ^{2}H(^{7}Be,d)^{7}Be reaction were detected in the MINI annular silicon strip detector with an inner radius of 2.4 cm and an outer radius of 4.8 cm divided into 16 1.5-mm strips. The detector was placed about 23 cm from the target covering forward laboratory angles $\approx$ 6° - 12° ($\approx$13° - 26° in the center of mass frame). See Figure 4.3 for a layout. Downstream an ionization chamber was implemented to diagnose the purity and intensity of the beam. The ionization chamber is a doubly segmented chamber filled with CF_4 gas, where particle identification can be accomplished by comparing the energy loss in the first segment to that of the total energy deposited. The pressure in the chamber can be adjusted so that the beam is completely stopped inside. As seen in Figure 4.4, a pure beam of ^{7}Be was achieved by stripping the beam to charge state q = 4^{+} at the terminal of the tandem accelerator.

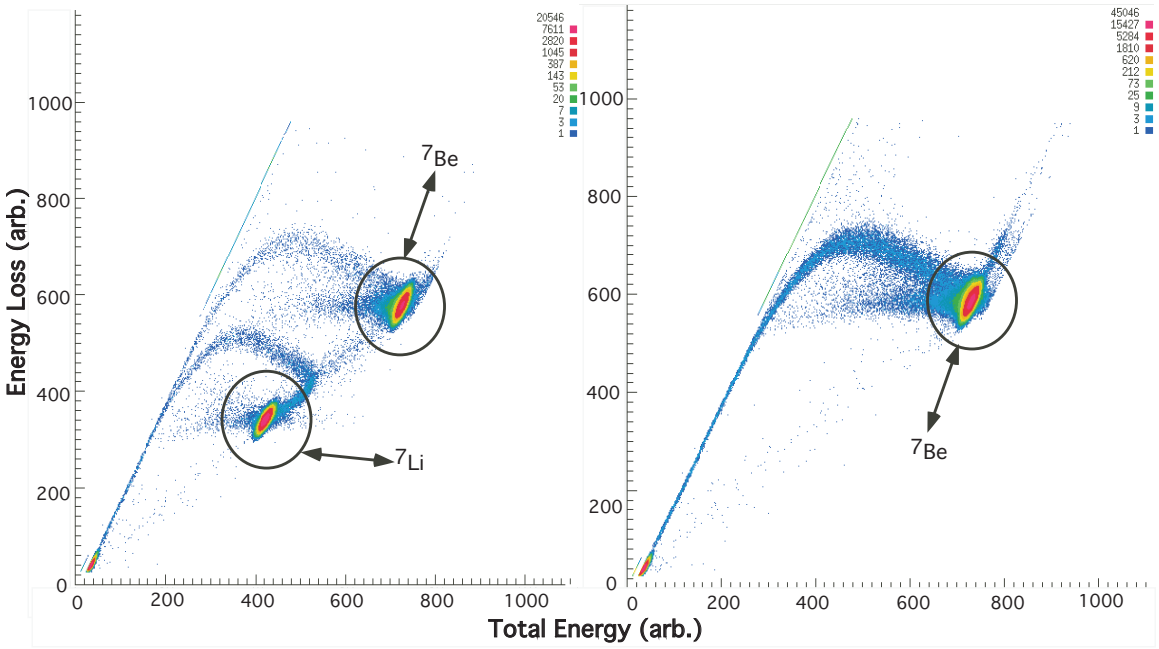

Figure 4.4: **(a)** Ion counter spectrum of energy loss as a function of total energy of the A=7 beam stripped to charge state 1^+. Note the presence of the ^{7}Li contamination. **(b)** Ion counter spectrum of beam stripped to charge state 4^+, indicating a pure ^{7}Be beam.

Because the energy of the proposed resonance was low ($E_{c.m.} \approx 200$ keV or $E_{^7Be} \approx 900$ keV), the scattered deuterons would also be low in energy ($E_d^{lab} \approx 600$ keV). Ideally the beam should be stopped near the back of the target to minimize the target energy loss of the outgoing deuterons. To reduce energy loss in the target, a target ladder was used that could rotate perpendicular to the beam line, effectively increasing the target thickness for the beam. With no rotation, the primary beam passed through the 1.62-mg/cm^2 target, losing most, but not all, of its energy, which was confirmed from spectra taken with the downstream ionization counter. The target was then rotated until no beam was detected in the ion chamber. The angle necessary for this was measured to be 50° ± 3°, giving an effective target thickness of 2.52 ± 0.15 mg/cm^2. The measured stopping thickness agrees with those calculated using the codes STOPIT (2.63 mg/cm^2)

and SRIM (2.52 mg/cm^2) [Bra78, Zie03]. Approximately 27 hours of data were taken during which 5×10^9 ions bombarded the CD_2 target.

4.3 Data and Analysis

Figure 4.5 shows an R-matrix calculation done for this measurement of the spectrum for the proposed resonance at $E_{c.m.} = 200$ keV with a width of 30 keV. A deuteron energy spectrum from a strip at 10.2° is shown in Figure 4.6. Comparing it to Figure 4.5, no obvious resonance is present. However, this spectrum is uncalibrated. Although no resonance is readily observed, there are corrections that need to be made to the data before conclusions can be drawn. As discussed above, this experimental method reduced the energy loss in the target; however it does not completely prevent it. Deuterons scattered at the resonance energy ($E_{c.m.} \approx 200$ keV) are still expected to lose about 50 keV of their 600 keV lab frame energy. This energy loss was estimated using a combination of kinematics codes RELKIN and STOPIT.

RELKIN is a code written in FORTRAN that calculates the energies of the outgoing particles as a function of angle for a particular nuclear reaction. It allows the user to input multiple beam energies as well as to specify the angular range of interest. STOPIT is another FORTRAN program written to estimate energy loss by a particle through a particular medium that is specified by the user. The medium can either be gas or solid and can have multiple layers. The user specifies the density, thickness, and composition of each layer and STOPIT will estimate the energy loss in each layer. Used in conjunction with RELKIN calculations, the energy loss of the deuterons in the target can be estimated.

First, STOPIT is used to determine the beam energy loss as it passes through the target. Next, RELKIN is used to calculate the outgoing energies of deuterons

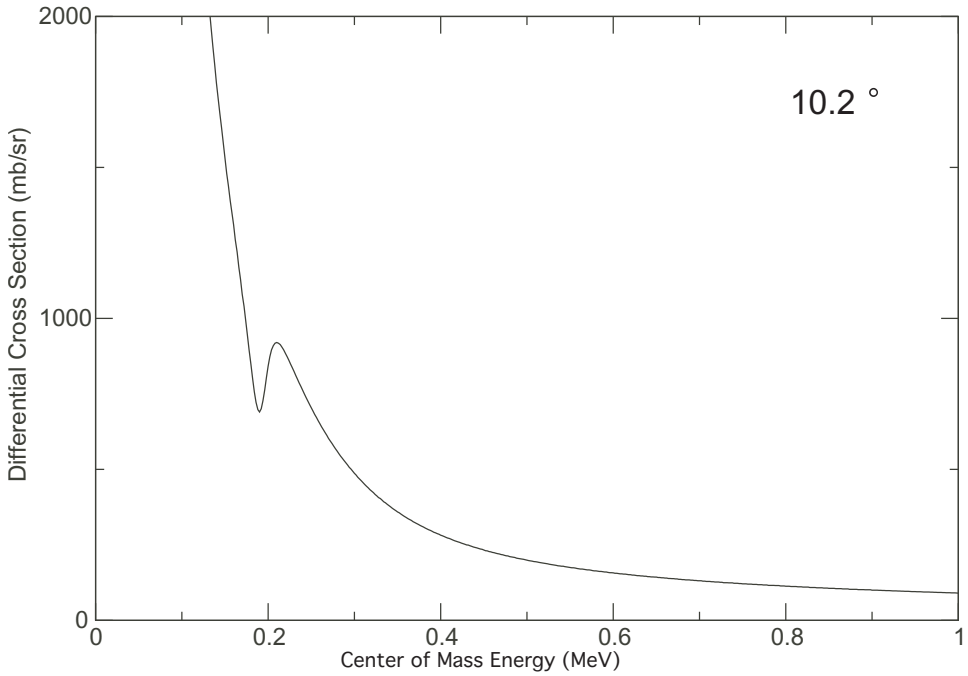

Figure 4.5: R-matrix calculation of the differential cross section as a function of energy using MULTI. A ^{7}Be+d resonance with $E_R \approx 200$ keV and $\Gamma \approx 30$ keV was assumed.

when the beam interacts at different points in the target at each strip angle. STOPIT is then used to estimate the energy loss of these deuterons as they pass through the remaining target material. In this way an estimate of the energy loss of the measured deuterons can be made by comparing the measured deuteron energies to those calculated by RELKIN for each angle covered by MINI.

The measured deuteron energy spectrum displayed in Figure 4.6 was corrected for the energy loss in the target and converted from the laboratory frame to the center-of-mass frame by using [Lee07]:

$$E_{c.m.} = \frac{m_d + M(^7Be)}{4M(^7Be)\cos^2\theta_{lab}} E_{d,lab}. \tag{4.1}$$

The spectra were then converted to differential cross sections using an energy-dependent target thickness Δx, which is inversely proportional to the stopping

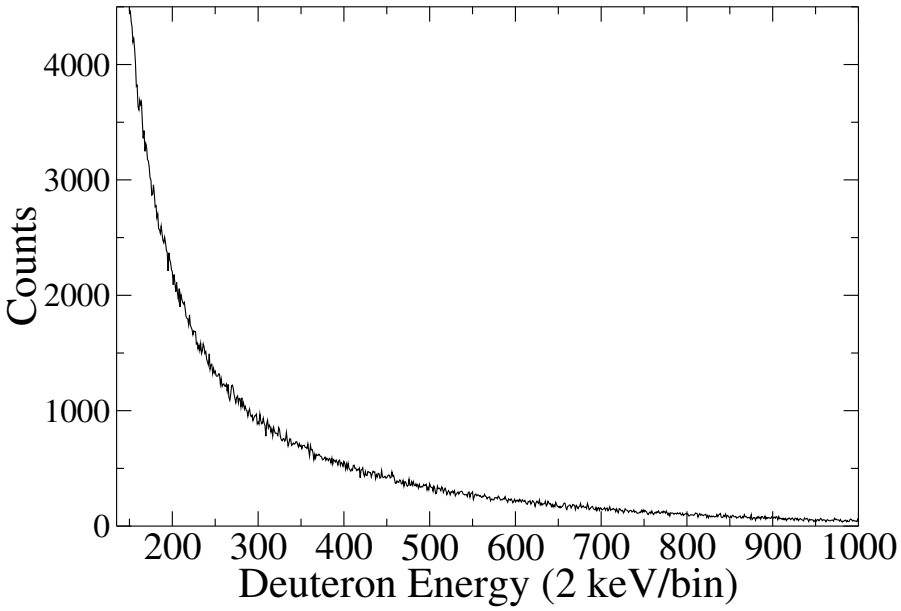

Figure 4.6: Counts as a function of deuteron energy measured in the laboratory in 2 keV intervals from the ^{7}Be(d,d) reaction at 10 MeV. The effective target thickness was 2.5 mg/cm^2. Data for a detector strip at 10.2° are shown.

power dE/dx:

$$\frac{d\sigma}{d\Omega} = \frac{R}{\rho \times \Delta x \times I \times \Delta\Omega} = \frac{R}{\rho \times (\Delta E \times \frac{dx}{dE}) \times I \times \Delta\Omega} = \frac{R \times \frac{dE}{dx}}{\rho \times \Delta E \times I \times \Delta\Omega} \tag{4.2}$$

where R is the deuteron yield, ρ is the target density, I is the time-integrated flux of ^{7}Be, $\Delta\Omega$ is the solid angle covered by the detector strip, and ΔE is the energy bin. This is the same method used in Reference [Lee07]. The stopping powers were estimated using SRIM [Zie03]. These data were then divided into 5 keV bins, and the resulting differential cross sections in the center of mass are displayed in Figure 4.7. Two MULTI R-Matrix calculations that were normalized to the data are also displayed in Figure 4.7.

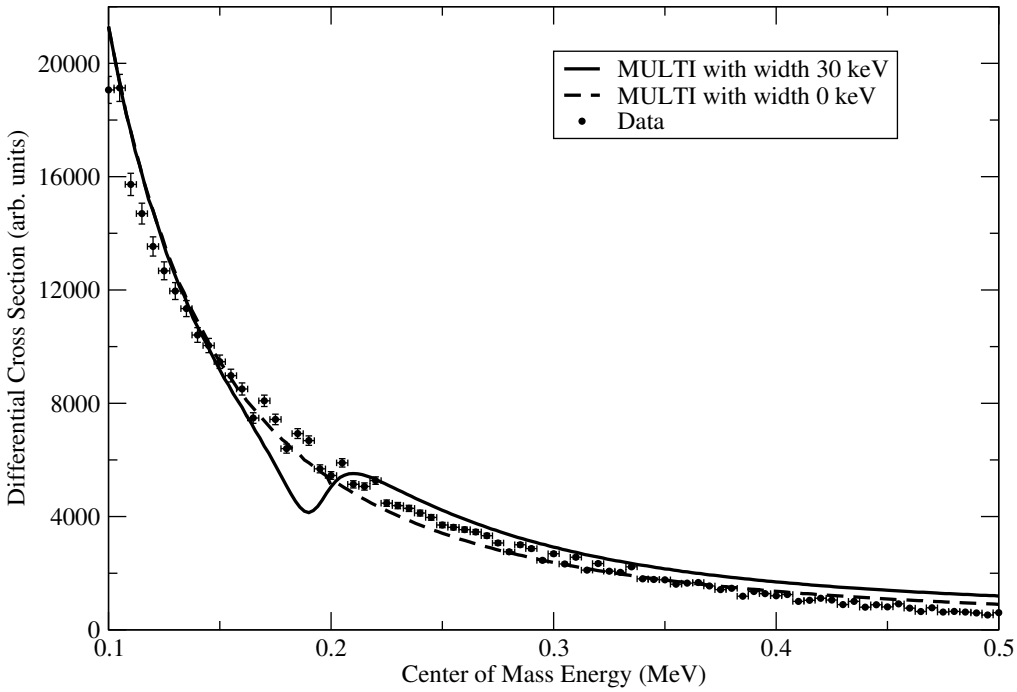

Figure 4.7: Differential cross sections as a function of center of mass energy for the ^{7}Be(d,d) reaction. Data are from the 10.2° detector strip shown in 5 keV bins. The solid line represents a MULTI calculation done assuming a resonance width of 30 keV. The dotted line represents a MULTI calculation done assuming a resonance width of 0 keV.

To interpret the data from the ^{7}Be+d measurement, R-matrix calculations for this experiment were performed with the FORTRAN code MULTI [Nel85]. This program computes R-Matrix cross sections for cases in which several channels may be open and several levels may be interfering with one another, although in the ^{7}Be+d study only the $5/2^+$ 16.7-MeV state in ^{9}B is considered. One thing to note is that MULTI views the entrance channel spin as simply the sum of the spins of the target and beam. The effects of the impact parameter are considered separately. The ground state of ^{7}Be has a J^π of $3/2^-$ and the deuteron has a J^π of

1^+ so the possible entrance channel spins used in MULTI are 1/2, 3/2, and 5/2. In the end a separate analysis must be done for each of these possible spins. This analysis can be simplified by remembering that an entrance channel spin of 1/2 would require an f-wave ($\ell = 3$) transfer to populate the resonance of interest. SInce this possible entrance channel spin was much less probable than the other two channels for which p-wave ($\ell = 1$) is allowed, $J = 1/2$ was neglected in this analysis. Figure 4.5 shows an example of a MULTI calculation done assuming a resonance energy of 200 keV and a width of 30 keV.

The results of the MULTI calculations were averaged over the laboratory energy resolution of 68 keV (22 keV in the center of mass), which is mostly due to the angular bin size and the intrinsic detector resolution. Looking at Figure 4.7, it appears that the best fit to the data is a calculation done assuming a zero width resonance. The lack of an obvious resonance implies that either the resonance does not exist or this experiment was not sensitive enough to observe it. So the only course remaining is to use MULTI to set upper limits (Γ^{max}) on a possible resonant contribution [Nel85].

The overall normalization of the MULTI calculations was allowed to vary as a free parameter and χ^2 fit tests were used to set upper limits on deuteron widths at a given confidence level. A resonance energy of $E_{c.m.} = 200$ keV was used for these calculations. Other resonance energies within the range from [Cyb09] were also explored, but no improvement was seen in the fit. Table 4.1 lists the results from the χ^2 analysis of the MULTI calculations for a few of the annular detector strips used in the present analysis. The upper limits were determined by increasing the resonance width from 0 (which had the lowest χ^2) until the χ^2 increased by 6.17, representing a 95.4% confidence level [Pre92]. The extracted upper limits from the individual strips were all about 1 keV.

Table 4.1: Upper limits Γ_d for the width of the possible ^{7}Be+d resonance at $E_{c.m.} \approx 200$ keV in ^{9}B. Upper limits were calculated for each detector strip. See text for details.

θ°_{lab}	Γ_d (keV) for entrance channel spin of 3/2	Γ_d (keV) for entrance channel spin of 5/2
6.9	1.1	1.1
7.3	0.4	0.5
7.7	0.6	0.7
8.0	1.1	1.2
8.8	0.8	0.8
9.1	0.8	0.9
10.2	1.5	1.6
11.0	2.4	2.4

4.4 Summary and Conclusions

It had been proposed that a $5/2^+$ resonance in ^{7}Be+d could resolve the ^{7}Li primordial abundance discrepancy. This resonance was searched for using the $d(^7\text{Be}, d)^7\text{Be}$ reaction with a 10-MeV rare isotope beam of ^{7}Be and a CD_2 target; no evidence for a resonance was observed. From analysis of the deuteron energy spectra with the R-matrix code MULTI, an upper limit of ~ 1 keV was deduced for a $5/2^+$ resonance in ^{7}Be+d corresponding to the 16.7-MeV state in ^{9}B. This upper limit is considerably lower than the minimum width of 10 keV that was proposed as a solution to the lithium abundance discrepancy [Pos11]. Therefore, other solutions to the cosmological ^{7}Li problem beyond the nuclear reaction rates should be pursued.

Chapter 5
Spectroscopic study of low-lying ^{16}N levels

5.1 Introduction

Understanding the origin of the elements and isotopic abundances in the universe is one of the main goals of nuclear astrophysics. After the Big Bang, most light nuclei are synthesized by fusion reactions between charged particles. While the probable production sites for many nuclei have been determined, many still remain a mystery. In particular, the nucleus ^{19}F may be produced on a side path of the CNO cycle described in section 1.2.3. However, the large cross section for the $^{19}\mathrm{F}(p,\alpha)^{16}\mathrm{O}$ reaction quickly destroys it in the proton-rich environment in stars. Currently, the astrophysical production site of galactic ^{19}F is uncertain. Possible sites include asymptotic giant branch (AGB) stars (stars burning ^{1}H in a shell but no longer in the core), supernovae, and Wolf-Rayet stars (very massive stars that rapidly lose their mass due to a strong stellar wind) [Wil02].

The only astrophysical site observationally confirmed to produce ^{19}F are AGB stars and they are considered the most likely source [Lug04]. Recent observations have found F overabundances of up to 250 times solar values in extremely hot post-AGB stars [Wer05]. However, model calculations have not yet been able to reproduce many observed abundance correlations, such as that of ^{19}F with ^{12}C [Lug04]. It is unclear the extent to which nuclear physics uncertainties are contributing to the discrepancies. Furthermore, in order to model ^{19}F production, a detailed understanding of the nuclear reactions occurring in the stellar

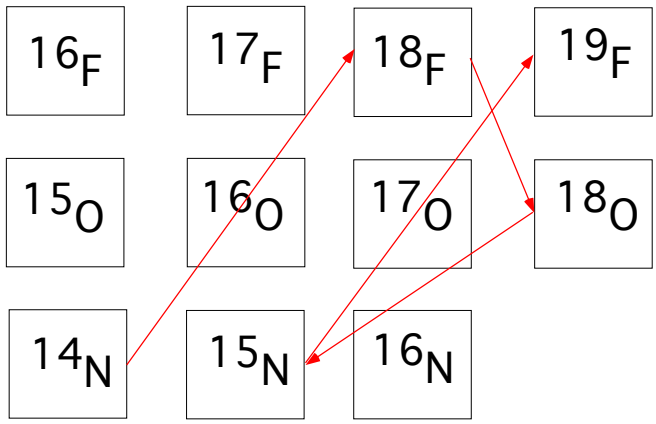

Figure 5.1: The sequence thought to be responsible for the production of ^{19}F in AGB stars. $^{14}\mathrm{N}(\alpha,\gamma)^{18}\mathrm{F}(\beta^+)^{18}\mathrm{O}(p,\alpha)^{15}\mathrm{N}(\alpha,\gamma)^{19}\mathrm{F}$.

site is needed. ^{19}F is thought to be produced in AGB stars via the sequence $^{14}\mathrm{N}(\alpha,\gamma)^{18}\mathrm{F}(\beta^+)^{18}\mathrm{O}(p,\alpha)^{15}\mathrm{N}(\alpha,\gamma)^{19}\mathrm{F}$ (see Figure 5.1).

It is important to consider the competition between different reactions that consume ^{15}N, such as the $^{15}\mathrm{N}(\alpha,\gamma)^{19}\mathrm{F}$ and $^{15}\mathrm{N}(n,\gamma)^{16}\mathrm{N}$ reactions, when calculating ^{19}F production. The $^{15}\mathrm{N}(n,\gamma)$ reaction is important as it would remove ^{15}N from the environment, leaving less available for the $^{15}\mathrm{N}(\alpha,\gamma)^{19}\mathrm{F}$ channel. While there has been considerable recent work studying the $^{15}\mathrm{N}(\alpha,\gamma)^{19}\mathrm{F}$ reaction [Wil02, For03, Deo97], there have been few studies of the $^{15}\mathrm{N}(n,\gamma)^{16}\mathrm{N}$ reaction. Reference [Mei96] estimated this reaction rate for the $^{15}\mathrm{N}(n,\gamma)^{16}\mathrm{N}$ reaction. The authors of this study found that the rate is dominated by p-wave ($\ell = 1$ transfer) direct capture over almost all of the relevant temperature range ($\approx 10^8 - 10^9$ K) with resonances only contributing at the highest of temperatures. The direct capture rate calculations depend directly upon the neutron spectroscopic factors of the states populated in direct capture. Thus a determination of the spectroscopic factors of low-lying ^{16}N levels is critical for calculating this rate.

There has been a single measurement of the neutron-spectroscopic factors for

low-lying ^{16}N levels [Boh72]. In this particular measurement, 5-6 MeV deuterium beams bombarded enriched-in-^{15}N melamine ($C_3H_6N_6$) targets. Protons from the (d,p) reaction were detected in silicon detectors. The ground state of ^{16}N and excited states at 120, 298, and 397 keV were observed. Each state had nearly equal spectroscopic factors of $\sim$0.5. Given that ^{15}N is a closed shell nucleus, this result was somewhat surprising. It was thought that low-lying ^{16}N levels were good single-particle levels with spectroscopic factors near unity [Mei96, Boh72]. These expectations were further confirmed by OXBASH calculations in Reference [Mei96] where spectroscopic factors between 0.87 and 0.96 were predicted. Additional information comes from a study of low-lying levels in the mirror nucleus, ^{16}F, where it was found that the observed properties of the mirror levels were only consistent with proton spectroscopic factors near unity [Lee07]. If isospin symmetry implies that the neutron spectroscopic factors in ^{16}N should be near unity. Furthermore, using the spectroscopic factors determined by [Boh72], the reaction rate of [Mei96] differs from that of a calculation done by [Rau94] by 30%. Clearly, the low spectroscopic factors for this nucleus need experimental confirmation.

5.2 Experiment

A new study of the ^{15}N$(d,p)^{16}$N reaction was performed at the ORNL HRIBF. An inverse kinematics study, $d(^{15}$N,$p)$, was chosen because enriched ^{15}N targets can be difficult to fabricate while CD_2 targets are readily available. Furthermore, to measure spectroscopic factors, one must measure the most forward center-of-mass angles where the cross section is most sensitive to the spectroscopic factors. In normal kinematics, (d,p) measurements can be difficult near 0° where the rate of elastically-scattered deuterons is high. However, in inverse kinematics forward

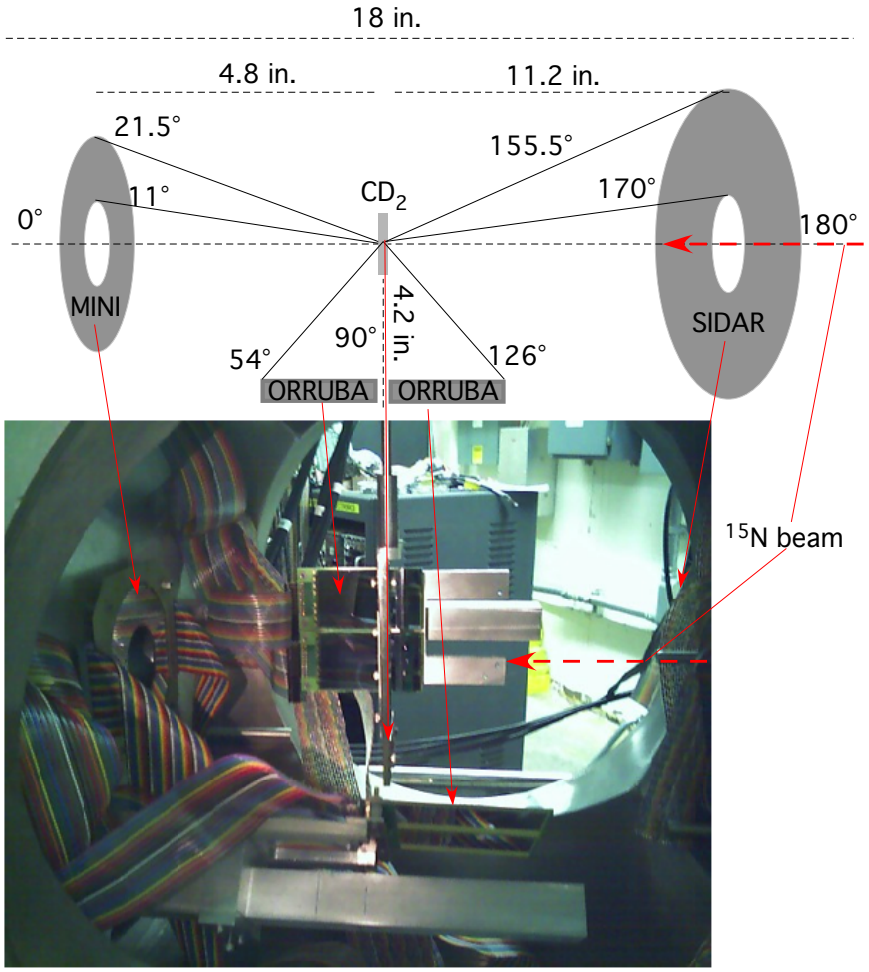

Figure 5.2: Experimental setup for the ^{15}N(d,p) reaction. Not shown is the Daresbury Recoil Separator that was downstream of the target chamber.

center of mass angles correspond to backward laboratory angles, where no elastic scattering would be observed.

A 100-MeV ^{15}N beam was used to bombard a 90-μg/cm^2 CD_2 target. Protons from the (d,p) reaction were detected at backward laboratory angles, 155°-169° (3°-8° in the center of mass frame) by the Silicon Detector Array (SIDAR) [Bar99]. To ensure that the identification of (d,p) protons was correct, some of the data were taken in coincidence with ^{16}N recoils that were transported and separated from the primary beam by the Daresbury Recoil Separator (DRS) [Jam88] and

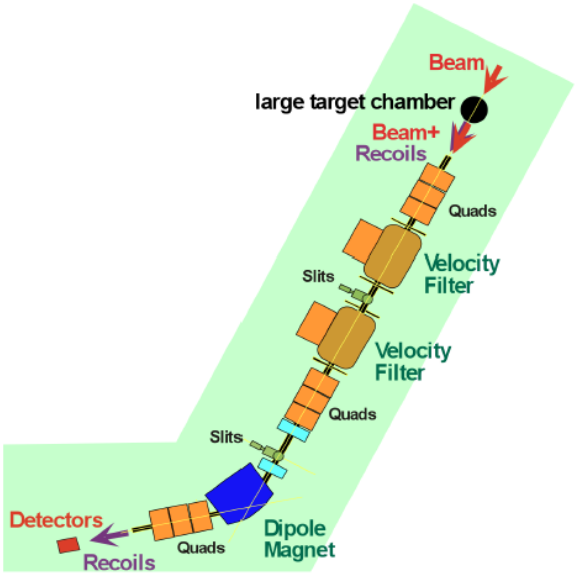

Figure 5.3: Schematic of the Daresbury Recoil Separator which is composed of a series of velocity filters for separating beam-like recoils. It can separate masses with a resolution $\Delta A/A \approx 1/100$.

detected in a silicon detector. The DRS has a mass resolution of $\Delta A/A \approx 1/100$ so it should be able to separate ^{15}N from other possible beam-like recoils.

The main purpose of detecting the recoils was to ensure that the protons from the ^{15}N(d,p) reaction were being correctly identified in the spectra. Figure 5.4 shows the spectrum from SIDAR in singles and in coincidence with ^{16}N recoils and demonstrates how cleanly the protons of interests can be identified. The results were enough to verify that the kinematics lines evident in the SIDAR spectra are from the states of interest.

Additional ORRUBA detectors were placed near 90° (θ_{lab} = 54° to 126° or θ_{cm} = 21° to 93°) and were useful for detecting reaction protons at larger center of mass angles and for monitoring target stability [Pai07]. The elastic scattering of deuterons from the target components during the run were recorded in ORRUBA (Fig. 5.8) and used to ensure target stability. The ORRUBA strips were oriented parallel to the beam axis such that the position along the strip of a detected

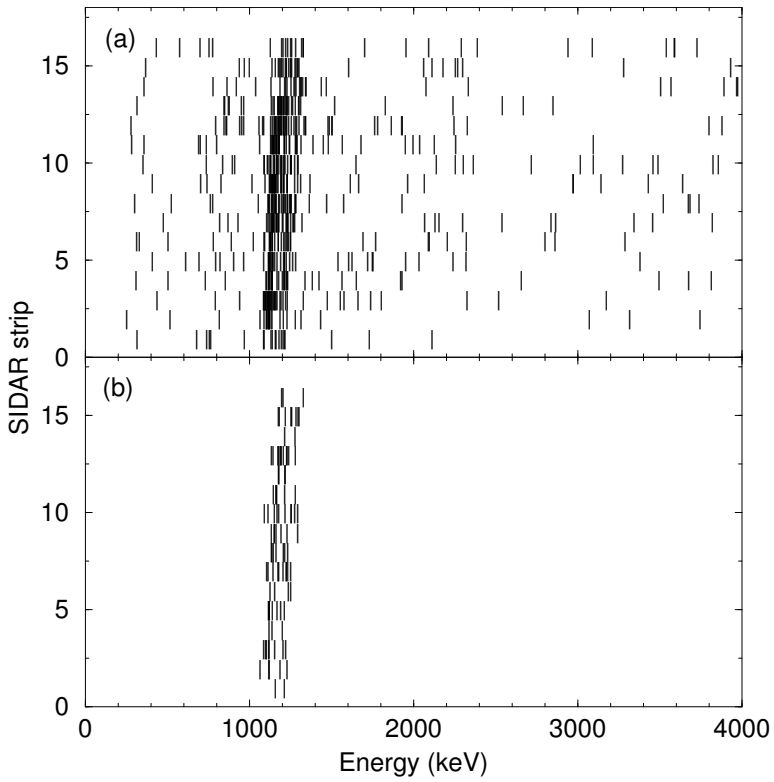

Figure 5.4: **(a)** Energy of detected particles observed in one SIDAR wedge. The laboratory angles range from 169° to 155° for strips 1 to 16, respectively. **(b)** Same as (a) but in coincidence with a ^{16}N recoil transported through the DRS. The band arising from $^{15}\mathrm{N}(d,p)^{16}\mathrm{N}$ is clearly identified.

particle provided a good measure of the polar angle (θ) of the reaction product.

Another smaller annular detector (MINI) was placed at forward angles (θ_{lab} = 9°-18°) to measure elastic scattering of the beam from the carbon in the target for beam current normalization. To determine this scattering rate, a silicon detector was inserted into the beam path downstream of the target location, and a low-intensity beam ($\sim 10^4$ particles per second) was counted while scattered beam particles were measured in the forward-angle detector. Afterwards, the beam detector was retracted, and the beam was raised to full intensity. Since the ratio of scattered particles to beam rate was determined, the elastic scattering could then be used as a measure of the beam rate. Typical beam intensities were kept

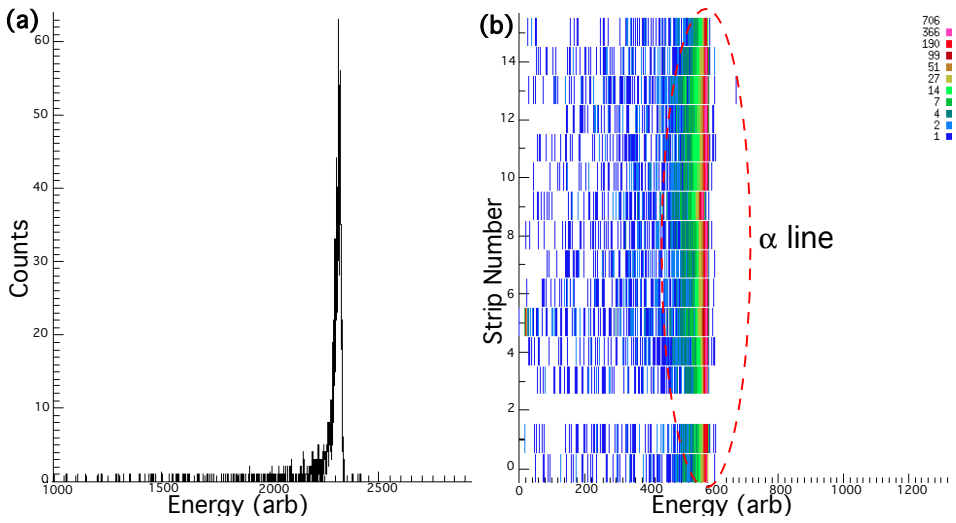

Figure 5.5: **(a)** Energy spectrum of one SIDAR strip from a 5.8 MeV alpha source. **(b)** The energy spectrum of the 5.8 MeV alpha source for one wedge of SIDAR.

below 3×10^6 ^{15}N/s to prevent target degradation. The lack of target degradation was verified by monitoring the rate of deuteron scattering in ORRUBA over time. Data were taken for approximately 65 hours and a total of 4.6 $\times 10^{11}$ ^{15}N ions impinged on the target over the course of the experiment.

5.3 Data and Analysis

5.3.1 SIDAR

The SIDAR analysis was actually done by Dan Bardayan from ORNL, but I will briefly discuss it here. SIDAR covered the most forward center of mass angles (3°-8°). An energy calibration for each strip of SIDAR was determined using a calibrated 5.8 MeV alpha source ^{244}Cm (shown in Figure 5.5). The activity of this source is known to be 3006 alphas per second into the full 4π. So, knowing the amount of time data were collected from the alpha source, the solid angle coverage of each strip can be determined. Once the solid angle has been determined and

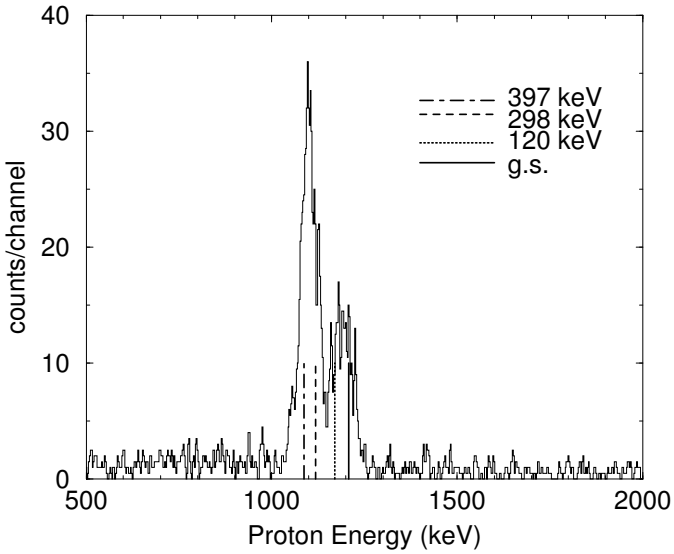

Figure 5.6: Singles energy spectrum observed in the inner strip of SIDAR. Lines show the expected positions of peaks from the ^{2}H(^{15}N,p)^{16}N reaction.

data from the strips calibrated, the strips of SIDAR at the same polar angle were summed over the azimuthal angle, ϕ. Figure 5.6 shows a typical singles spectrum from one of the SIDAR strips. As can be seen in Fig. 5.6, there was relatively little background in the spectra, and thus background subtraction was straightforward. To extract the cross sections from these low-lying ^{16}N levels, the standard equation 4.2 was used. The differential cross sections from SIDAR are shown later in Figure 5.11. The uncertainties shown on the data points are purely statistical.

5.3.2 ORRUBA

ORRUBA covered angles further back in the center of mass frame than SIDAR from $\theta_{cm} = 21^{\circ}$ to 93°. The calibration of ORRUBA took place in two stages. First, an energy calibration was done using the plot shown in Figure 5.7**a**. Each end is gained matched so that a particle interacting at the center of the strip

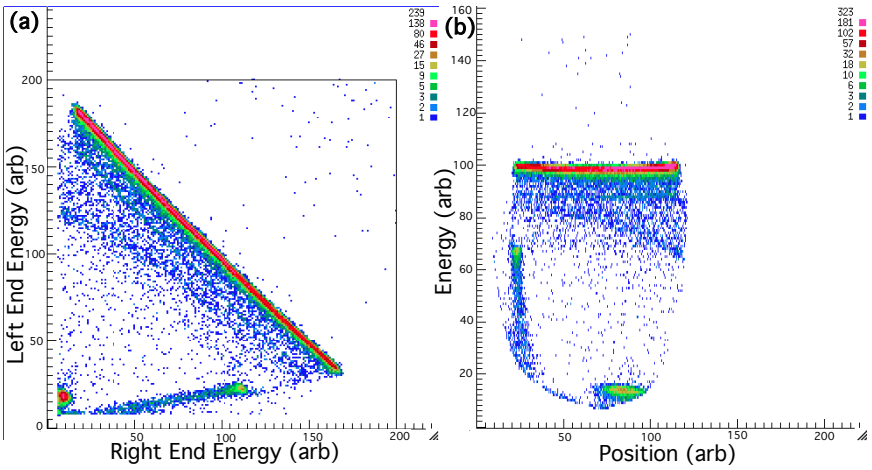

Figure 5.7: **(a)** The energy read from one end of an ORRUBA strip vs the energy deposited by the opposite end for a 5.8 MeV alpha source. **(b)** The energy measured by one ORRUBA strip plotted against the position for the 5.8 MeV alpha source.

will produce an equal signal in both ends. Next a position calibration is done using Figure 5.7**b**. The alpha source should trigger events throughout the entire length of the ORRUBA strip, so that the length of the alpha line in this spectrum should represent the length of the strip. Making this calibration allows for the exact position (as well as the angle) of each event to be determined. Details on the position and angle calculation are presented in section 3.2.

Figures 5.8 and 5.9 show ORRUBA Energy vs Position spectra for a forward laboratory angle ORRUBA strip and a backward laboratory angle ORRUBA strip for the ^{15}N(d,p) measurement. Notice in both spectra how clearly the kinematics line from (d,p) is identified. The ORRUBA data were then summed over ϕ into 2° bins of θ. Figure 5.10 shows one such bin, located at $\theta_{lab} = 110°$. As in the SIDAR data, there are two doublets, one representing the ground state and 120-keV state and one representing the 298-keV and 397-keV states. Cross sections for each doublet were derived as with SIDAR using formula 4.2. The angular distribution is plotted along with that observed in SIDAR in Figure 5.11.

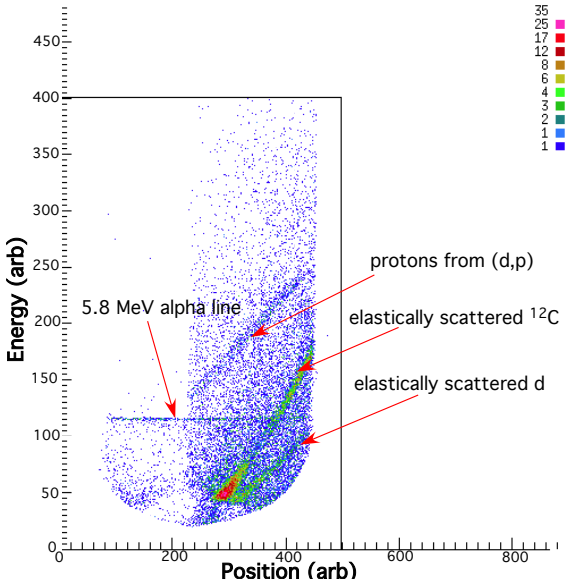

Figure 5.8: Energy vs. position for events observed in one strip of ORRUBA detector placed near 90°. 90° is at ≈ position 220, with increasing position representing forward laboratory angles.The scattering of target constituents is noted at positions $\theta_{lab} \geq 90°$. The reduction of counts backwards of 90° arises from target-frame shadowing.

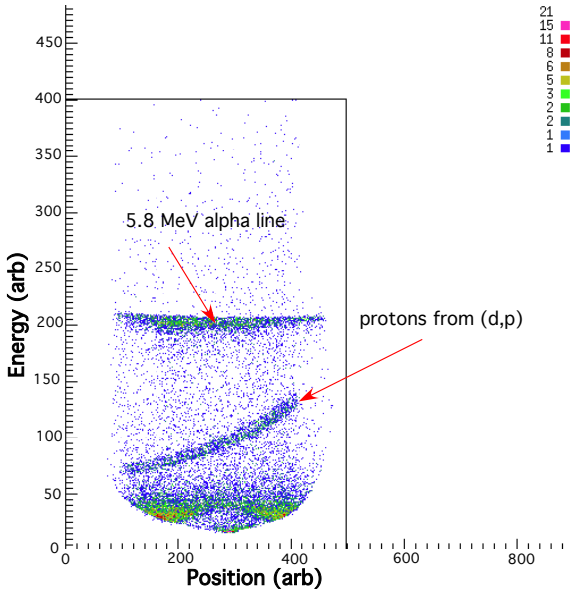

Figure 5.9: Detected energy vs. position spectrum for a portion of the events observed in an ORRUBA detector placed from 90° to 126°. Note that the absence of elastically scattered particles.

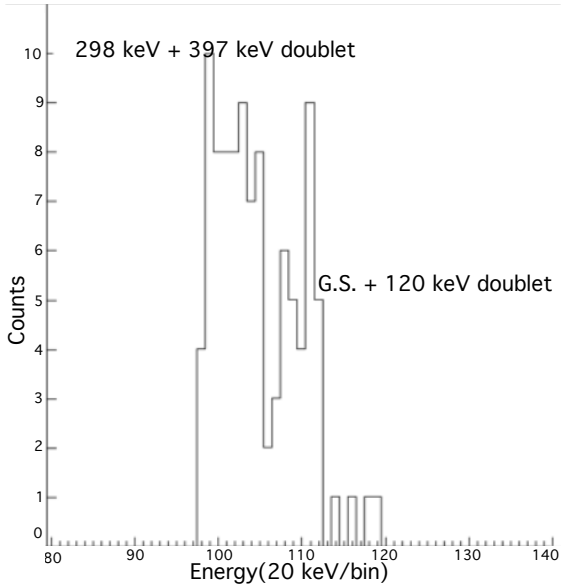

Figure 5.10: Data from a 2° ORRUBA bin located at $\theta_{lab} = 110°$, summed over ϕ.

5.4 Results

In Figure 5.11, the angular distribution for the ^{15}N(d,p) reaction populating two doublets. These doublets correspond to states at 0+120 keV and 298+397 keV. The data are plotted along with DWBA calculations performed using the code TWOFNR [Igar]. The global optical model parameters of Perey and Perey were found to be suitable for the Woods-Saxon potential of Section 2.2.2 and implemented [Per76]. These parameters are listed in Table 5.1. Since individual states were not separated in these data, the DWBA calculations were combined using two methods.

The first method used the relative spectroscopic factors for the four states reported in Bohne *et al.* to weight the DWBA calculations and the overall magnitude was allowed to vary in the fit [Boh72]. Even if the magnitudes of these values are not correct, it is likely that the relative strengths are valid. In the

Table 5.1: Global optical model parameters of [Per76] used in the Woods-Saxon potential (shown in Section 2.2.2) for the DWBA calculations. The parameter V definitions follow the normal conventions and correspond to those found in [Per76]. For the neutron n, V was fit to reproduce the binding energy of the neutron. In all cases, $W = 0$ MeV. Note that ^{15}N has a ground state spin of 1/2.

	V (MeV)	r_0 (fm)	a_0 (fm)	W_D (MeV)	r_W (fm)	a_W (fm)	V_{so} (MeV)	r_{so} (fm)	a_{so} (fm)	r_C (fm) height
^{15}N+d	85.31	1.15	0.81	16.0	1.34	0.68	0.0	1.0	1.0	1.15
^{16}N+p (g.s)	54.19	1.25	0.65	13.5	1.25	0.47	7.5	1.25	0.47	1.25
n	-	1.25	0.65	0.0	-	-	6.0	1.25	0.65	1.25

second method, the magnitudes of each DWBA component were allowed to vary as a free parameter. The spectroscopic factors from both methods were determined using methods discussed in section 2.2.3 and are listed in Table 5.2. The systematic uncertainties in the spectroscopic factors are estimated to be about 15% resulting mostly from uncertainties in the target thickness ($\sim$ 11%) and beam current normalization ($\sim$ 10%). Additional model uncertainties are not considered as they will likely have a negligible effect on the overall uncertainty. For comparison, previous results from Bohne *et al.* and OXBASH shell model calculations are also included [Boh72]. Both methods for determining the spectroscopic factor used in this dissertation produced reasonable fits to the data and spectroscopic factors that agreed much better with the near-unity OXBASH calculations [Mei96]. Notice that the spectroscopic factors of our measurement differ from Bohne *et al.* by about a factor of 2.

The differences in the spectroscopic factors from this work and those extracted by Bohne *et al.* are doubtfully the result of using different optical model parameters [Boh72]. We were able to reproduce the DWBA calculations of Bohne *et al.* using the parameters in Table 5.1 which supports the notion that the cause of the discrepancy comes from the data [Boh72].

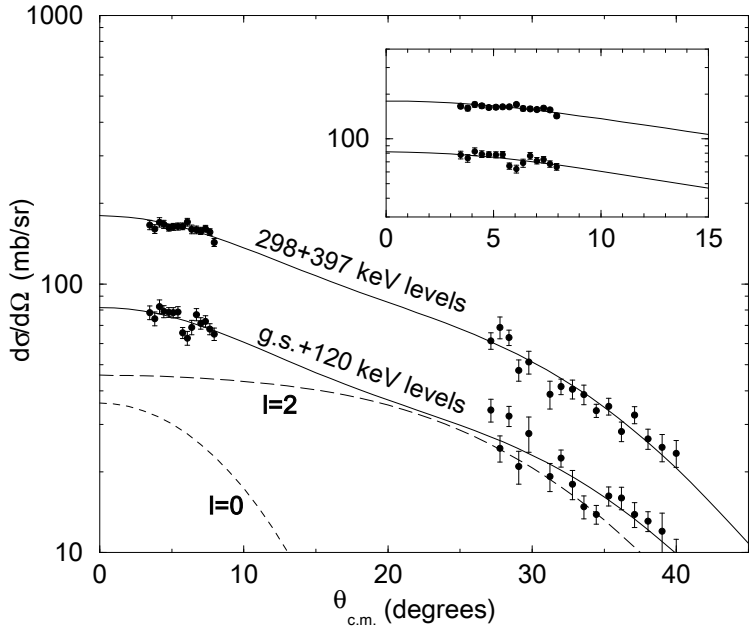

Figure 5.11: Differential cross sections for the ^{15}N$(d,p)^{16}$N reaction as a function of center-of-mass angle. The inset shows an expanded view of the SIDAR data. Since resolution of the closely-spaced levels was not possible, composite DWBA curves have been fitted to the data. Here the magnitudes of the DWBA calculations were allowed to vary as free parameters and fit to the data. The dashed curves show the contributions that were summed to fit the g.s. + 120-keV cross sections.

5.5 Summary and Conclusions

There has been a long-standing discrepancy between the measured neutron spectroscopic factors for ^{16}N and the expected values [Mei96, Boh72, Lee07]. Spectroscopic factors have a direct impact on the calculated ^{15}N$(n,\gamma)^{16}$N reaction rate, which is of importance to nucleosynthesis calculations of ^{19}F in AGB stars. A re-measurement of the ^{15}N$(d,p)^{16}$N reaction was performed using inverse kinematics with the SIDAR and ORRUBA arrays in conjunction with the DRS. It was found that the neutron spectroscopic factors are consistent with near-unity expectations from shell model calculations.

With this work, the ^{15}N$(n,\gamma)^{16}$N reaction rate of [Mei96] has been updated using the average of the spectroscopic factors listed in the last two columns of Table 5.2. The

Table 5.2: Spectroscopic properties of ^{16}N excitations in comparison with shell model predictions [Mei96]. The last two columns show the results of the present work when the magnitudes of the individual components were fixed to the ratios of spectroscopic factors from Reference Bohn *et al.* or were allowed to vary freely, respectively. OXBASH calculations for spectroscopic factors were adopted from Meissner *et al.* [Boh72, Mei96]. Statistical uncertainties are given in parenthesis. The systematic uncertainties are estimated to be ∼15%.

E_x(MeV)			C^2S	C^2S	C^2S	C^2S
	J^π	nl_j	[Boh72]	OXBASH	present[1]	present[2]
0	2^-	$1d_{5/2}$	0.55	0.93	0.96(2)	1.04(4)
0.120	0^-	$2s_{1/2}$	0.46	0.95	0.80(1)	0.71(6)
0.298	3^-	$1d_{5/2}$	0.54	0.87	0.91(1)	1.03(3)
0.397	1^-	$2s_{1/2}$	0.52	0.96	0.88(1)	0.74(5)

[1]Ratio of components constrained in fit
[2]Components allowed to vary freely

^{15}N$(n,\gamma)^{16}$N reaction rate is dominated by p-wave direct capture to low-lying ^{16}N levels. The calculated p-wave contribution depends directly on the measured spectroscopic factors and thus it was scaled from Reference [Mei96]. The s-wave contribution is strongly-inhibited; an estimate of its strength from Reference [Fow67] is also displayed. The major resonance contribution comes from the 862-keV resonance. The contribution of this resonance is taken unchanged from Reference [Mei96]. The resulting reaction rate is plotted in Fig. 5.12 and is given by the expression

$$\begin{aligned} N_A < \sigma v > &= 3.18 + 5.29 \times 10^3 T - 715 \times T^{1.7} + \\ &\quad 5.3 \times 10^5 T^{-3/2} \exp(-10.0/T) \end{aligned} \tag{5.1}$$

where the rate is given in cm^{3}mole^{-1}s^{-1}, N_A is Avagadro's number, and the temperature is given in GK. The calculated ^{15}N$(n,\gamma)^{16}$N reaction rate is about a factor of 2 larger than the rate from Reference [Mei96] due to the larger spectroscopic factors used in the current calculation. These increased spectroscopic factors will lower the amount of ^{15}N available to produce ^{19}F through the ^{15}N$(\alpha,\gamma)^{19}$F reaction and thus lowers the abundance of ^{19}F predicted by models. Unfortunately, this does not resolve the discrepancy between model calculations and observations for the abundance of ^{19}F in post-AGB stars.

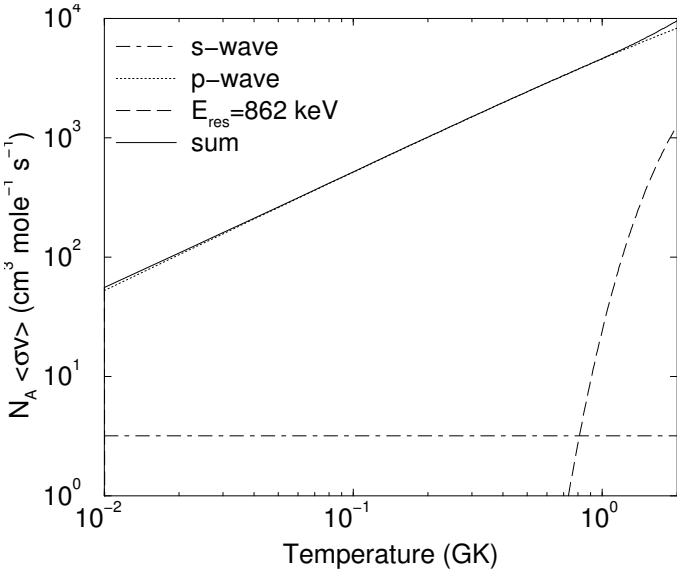

Figure 5.12: $^{15}\mathrm{N}(n,\gamma)^{16}\mathrm{N}$ rate as a function of stellar temperature in GK. The rate is dominated by p-wave direct capture.

Chapter 6
^{20}Ne(p,d) and the astrophysical ^{18}F mystery

6.1 Introduction

Gamma-ray emission from novae is dominated by e^+e^- annihilation. The positrons necessary for this interaction typically result from the β^+ decay of radioactive nuclei during the first few hours following the initiation of the outburst. These positrons could come from a variety of sources, but ^{18}F is considered a primary candidate because of its long half-life ($t_{1/2} \approx 110$ min.) and its relatively high abundance. If satellites such as INTEGRAL detected the ^{18}F gamma-rays, it would provide a direct test of nova models [Her99, Her01]. To date, gamma-rays associated with nova outbursts have not been observed. One of the major challenges is that the sensitivity requirements and maximum detection distances are poorly known due to uncertainties in the nuclear processes that govern the creation and destruction of ^{18}F. In particular, the ^{18}F$(p,\alpha)^{15}$O reaction is thought to destroy a significant fraction of the ^{18}F nuclei before they are carried by convection to the top of the explosion envelope. This rate significantly affects the net abundance of ^{18}F for gamma-ray emission.

Several experiments have been done to better understand this important reaction rate [Bar02, Koz06, Ser07, Ser09]. These results indicated a large amount of s-wave (i.e. $\ell = 0$) strength concentrated near the proton threshold in ^{19}Ne. Depending on whether these strong single-particle levels are above or below the proton threshold of ^{19}Ne, the calculated ^{18}F(p,α) rate could change dramatically. Resonances that lie just below the proton threshold, especially those with low ℓ transfer, may also significantly affect the ^{18}F$(p,\alpha)^{15}$O reaction rate due to their large alpha width. A large alpha width implies

that the state will likely decay as an alpha particle. As a result of these uncertainties in the reaction rate, the predicted amount of ^{18}F produced in nova explosions is poorly known.

An experiment was performed at ORNL to measure the proton transfer to states in ^{19}Ne using a beam of ^{18}F bombarding a CD_2 target [Ade11]. The properties of several resonances were measured and the results are shown in Table 6.1. There appears to be a $\ell = 0$ state just below the threshold that could potentially have a significant contribution to the reaction rate, depending on its spin. With the ground state $J^\pi = 1^+$ of ^{18}F and an $\ell = 0$ transfer into the 6.289-MeV state, the final spin could be either $1/2^+$ and $3/2^+$. This difference is significant because the alpha width is estimated from the mirror, but mirror assignments are difficult if the spin is not known. In fact, it was estimated by Adekola *et al.* that the width is 11.62 keV if the spin is $1/2^+$ but 0.44 keV if the spin is $3/2^+$ [Ade11]. It is therefore important that the spin of this sub-threshold resonance be determined.

A possible probe of the spin of this state could come from a study of the ^{20}Ne$(p, d)^{19}$Ne reaction. The state would be populated by an $\ell = 0(2)$ transfer if its spin is $1/2^+(3/2^+)$. These differing ℓ transfers would produce different angular distributions for the outgoing deuterons, and thus a measurement of these angular distributions would determine the spin of this important state.

6.2 Experiment

At ORNL, the ^{20}Ne(p, d) reaction was measured to determine the spin of the 6.289-MeV sub-threshold state. The measurement was performed in normal kinematics, using a 30-MeV proton beam. The ^{20}Ne material was implanted into a carbon foil. However, the actual amount of ^{20}Ne in the target was poorly known. A "pure" carbon foil was also bombarded to identify contaminants and therefore help to identify the peaks corresponding to states populated in ^{19}Ne. Outgoing particles were detected downstream

Table 6.1: Resonance parameters used in the calculation of $^{18}\mathrm{F}(p,\alpha)^{15}\mathrm{O}$ astrophysical S-factor and reaction rate. Taken from [Ade11].

E_r (keV)	J^π	Γ_p (keV)	Γ_α (keV)
-122	$1/2^+$ or $3/2^+$	-	11.62 or 0.44
8	$3/2^-$	1.27×10^{-38}	0.27
26	$1/2^-$	1.1×10^{-20}	220.0
38	$3/2^+$	2.35×10^{-15}	4.0
287	$5/2^+$	1.2×10^{-5}	1.2
330	$3/2^-$	2.22×10^{-3}	2.7
450	$7/2^-$	1.6×10^{-5}	3.1
665	$3/2^+$	15.2	24.0
827	$3/2^+$	0.35	6.0
842	$1/2^+$	0.2	23.0
1009	$7/2^+$	27.0	71.0
1089	$5/2^+$	1.25	0.24
1122	$5/2^-$	10.0	21.0

by the annular SIDAR detector array in its lampshade configuration, which is comprised of 6 silicon strip wedge-shaped telescopes [Bar99]. Each telescope consisted of a 65-micron 16-strip ΔE detector with a 300-micron residual E 16-strip detector (see Figure 6.1). Particle identification was accomplished by plotting the energy deposited in the thin detector vs the total energy deposited by the particle. Figure 6.2 shows an example of these spectra. Many channels were open in this reaction induced by high energy protons. Therefore gating on the particles of interest, deuterons in this case, was important before analyzing the energy spectra.

6.3 Data

Figure 6.3 shows a deuteron energy spectrum from one strip. The angular region SIDAR covered in this measurement was fairly broad ($\theta_{lab} = 29^\circ - 73^\circ$). However a complication arose that prevented the 6.289-MeV state in ^{19}Ne from being clear over this entire range. In Figure 6.3 other nuclei appear to be present in the target besides carbon and neon, most important of which is oxygen and silicon. The oxygen is from

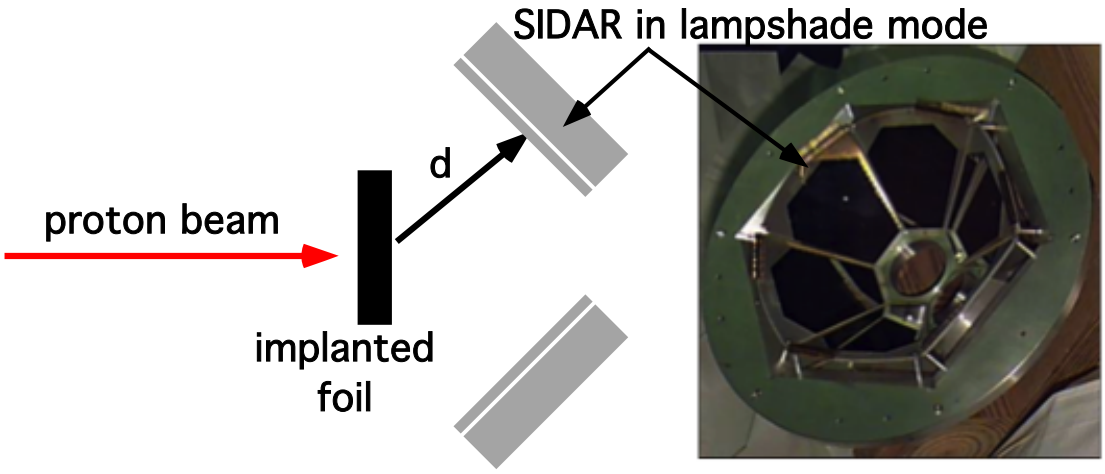

Figure 6.1: Diagram of the experimental setup. To the right is a photograph of SIDAR in its lampshade configuration.

water in the air that had been absorbed into the carbon foil but the silicon came from a previous measurement in which this target was bombarded by a beam of ^{28}Si. The states were deduced by their kinematic curves. In addition to the expected ^{12}C(p,d) peaks, ^{16}O(p,d) peaks were also visible. Peaks from the oxygen contaminants limited the angular range in which the state of interest could be observed. However the peaks from states populated in ^{11}C are quite useful. Since this nucleus has been studied in much detail, the excitation energies of its states are well known; these peaks can therefore be used as an internal energy calibration.

As can be seen in the photograph of the ^{20}Ne implanted target in Figure 6.4, the target thickness would have been difficult to determine and the actual density of ^{20}Ne is not known. However, the final spin can be determined because the shape of the angular distributions from the two possible angular momentum transfers are different. Figure 6.5 shows Distorted Wave Born Approximations (DWBA) calculations for the ^{20}Ne(p,d) reaction done using the code TWOFNR [Igar].

^{20}Ne is a deformed nucleus, meaning that it does not have the spherical shape assumed by most global optical model parameters [Bar67]. Therefore, it is important to get an appropriate set of optical model parameters rather than using a global set such

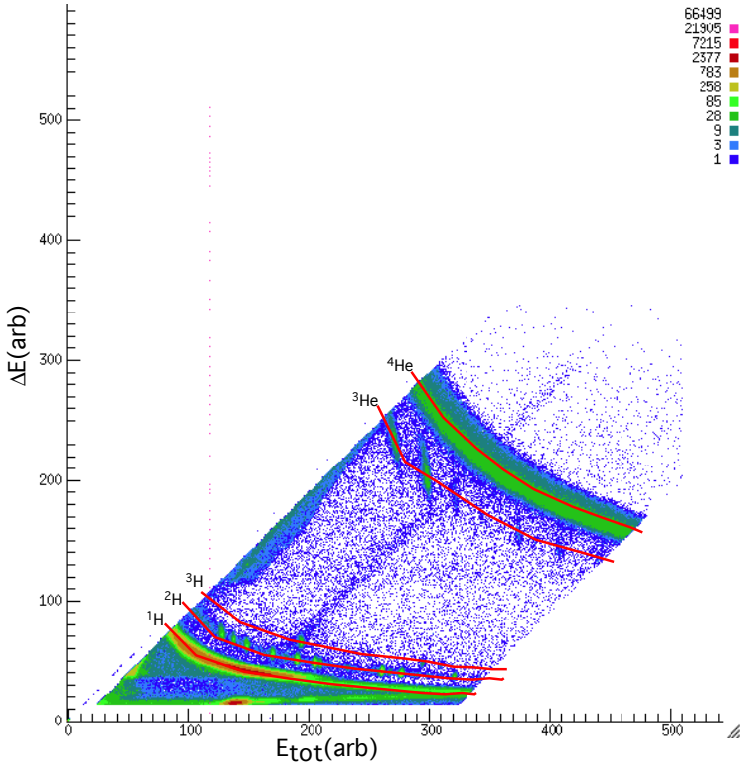

Figure 6.2: Particle identification from one SIDAR telescope. The energy deposited in the thin detector (ΔE) is plotted against the total energy deposited (E).

as Perey that assume a spherical nucleus [Per76]. Table 6.2 displays the optical model parameters that were taken from [Koz06] and scaled for this measurement. Figure 6.5 demonstrates that the shapes of the distributions for the two potential ℓ transfers in the region covered by SIDAR are quite different. So the shape of the angular distribution can be used to determine the spin of the state.

As was clear in Figure 6.3, there are several very strong peaks in ^{15}O that come from water that had been absorbed by the target. In particular, the peak of interest becomes obscured by deuterons populating the 6.793-MeV state of ^{15}O. Figure 6.6 shows how the states become inseparable at higher angles. Because of this fact considerably the effective range of SIDAR in this measurement was reduced to $\theta_{lab} = 30.3^\circ - 45.0^\circ$ ($\theta_{cm} = 33.2^\circ - 49.2^\circ$).

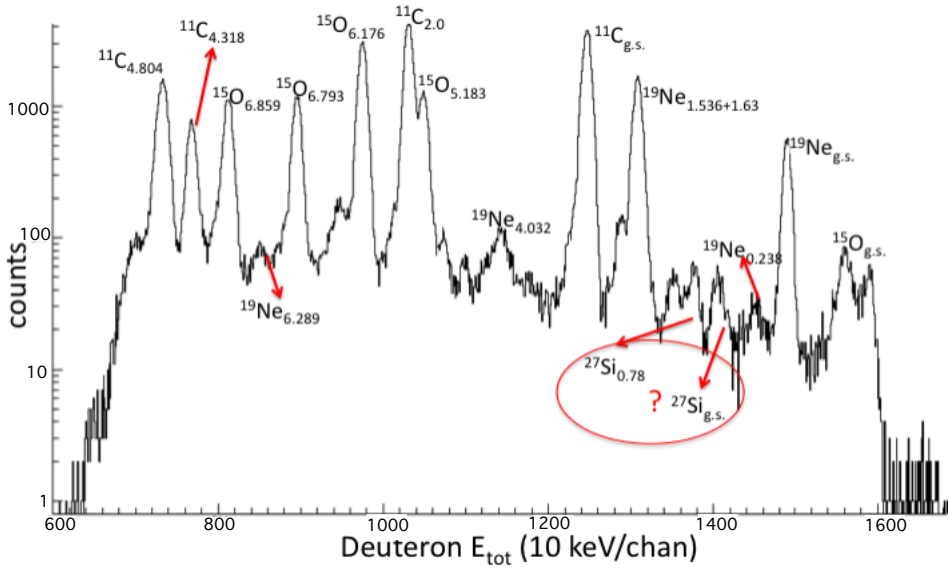

Figure 6.3: Spectrum from one strip of SIDAR, gated on the deuteron curve from Figure 6.2. The assignments for each peak are based on kinematics and alpha source energy calibration. The carbon peaks were later used to refine the energy calibration.

Table 6.2: Optical Model parameters for the deformed nuclei ^{19}Ne and ^{20}Ne, taken from [Koz06]. These parameters were used in DWBA calculations using the Woods-Saxon potential of section 2.1.2.

Particle	V_R (MeV)	r_R (fm)	a_R	$4V_l$ (MeV)	r_l (fm)	a_l (fm)	r_c (fm)
^{20}Ne+p	52.4	1.356	1.01	10.4	1.474	0.64	1.39
^{19}Ne+d	109	1.349	0.70	58.8	1.385 7	0.60	1.39

6.4 Results

Figure 6.7 shows TWOFNR calculations for $\ell = 0$ and $\ell = 2$ transfer normalized to the data to determine if a final spin assignment can be made in this restricted angular range. The calculations were fit to the data using a least χ^2 routine allowing the normalization to vary as a free parameter. The best χ^2 for each fit were 11.9 and 4.7 for the $J = 1/2$ and $J = 3/2$ spin assignments, respectively. Based on this, a spin assignment of 3/2 would seem appropriate. However, while the data do appear to follow the $\ell = 2$ calculations better, both ℓ transfer calculations are relatively flat in the region around the data. Furthermore, the last data point located at $\theta_{c.m.} = 50.2°$

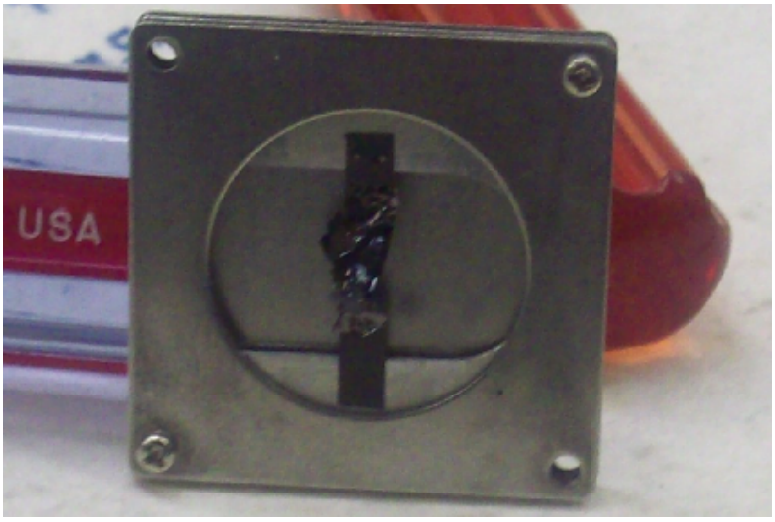

Figure 6.4: Carbon target implanted with ^{20}Ne. The target thickness was difficult to determine due to the poor quality of the target.

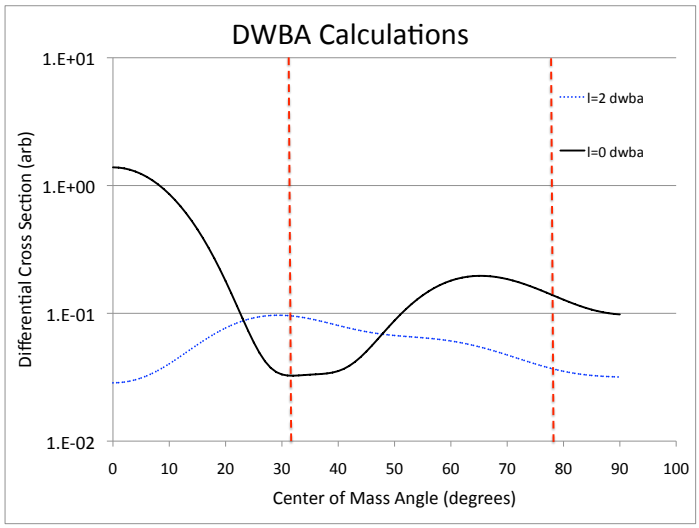

Figure 6.5: DWBA calculations of differential cross sections for $\ell = 0$ and $\ell = 2$ transfer to the 6.289-MeV state in ^{19}Ne from TWOFNR scaled to the data. The angles between the dashed red lines represent those covered by SIDAR in the present setup.

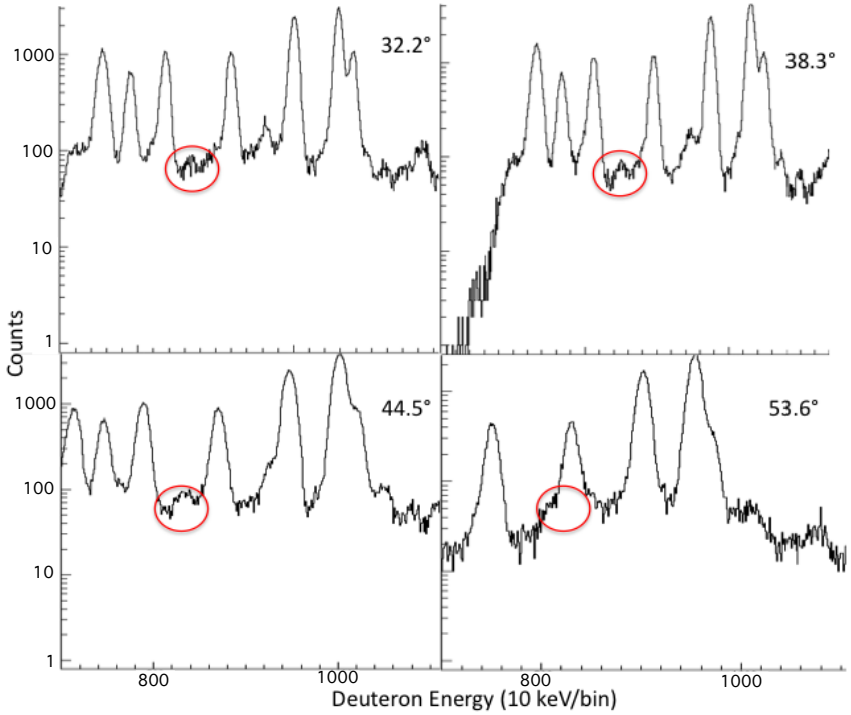

Figure 6.6: Deuteron energy spectra from several strips in SIDAR. The state of interest is the 6.289-MeV state of ^{19}Ne and is circled. Note how the state of interest is obscured by the stronger peak from a state in ^{15}O.

shows that the differential cross section might be starting an upward trend. If that were the case, then an the $\ell = 0$ calculation might fit the data better. The result is that no spin assignment can be made with confidence. A definite spin assignment could have been made if either a larger angular range was observed, or the target had been free of contamination.

6.5 Summary and Conclusions

Gamma-ray emission in novae is dominated by positron-electron annihilation. ^{18}F, due to its long half life (110 min) and high abundance, has been considered the most likely source of positrons. However, gamma rays from this nucleus have not yet been observed. In order to understand reactions that affect ^{18}F abundances in novae, a measurement was done by [Ade11] to determine the properties of resonances near the

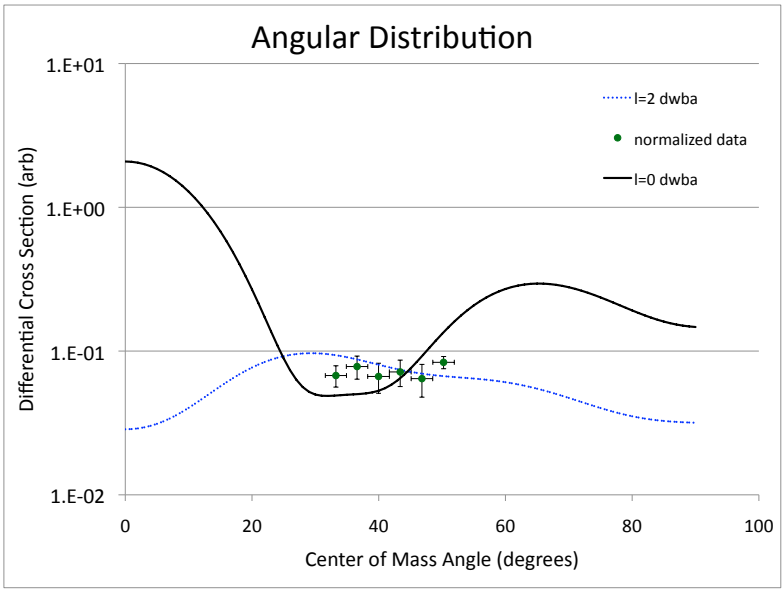

Figure 6.7: Differential cross sections as a function of center of mass angle for the 6.289-MeV state in ^{19}Ne from the ^{20}Ne(p,d) reaction. Also plotted are TWOFNR DWBA calculations for differential cross section that were normalized to the data by a reduced χ^2 routine.

proton threshold. One sub-threshold state could have a strong effect on the ^{18}F(p,α) reaction rate, but its spin has not been determined. To determine the spin of this 6.289-MeV state, a 30-MeV proton beam bombarded a carbon foil implanted with ^{20}Ne. Outgoing particles were detected in the SIDAR array and an angular distribution from the ^{20}Ne$(p,d)^{19}$Ne reaction was extracted. An absolute normalization of this reaction was not possible and the contaminants in the target prevented the state of interest from being observed over much of SIDAR's angular coverage. As a result, no spin assignment could be made.

Since the results of this study proved inconclusive, another measurement is necessary. The major difficulty in this experiment was the contamination in the target. A pure target would prevent contamination and enable an absolute normalization. However, a pure neon target requires a gas target implementation. A major difficulty with

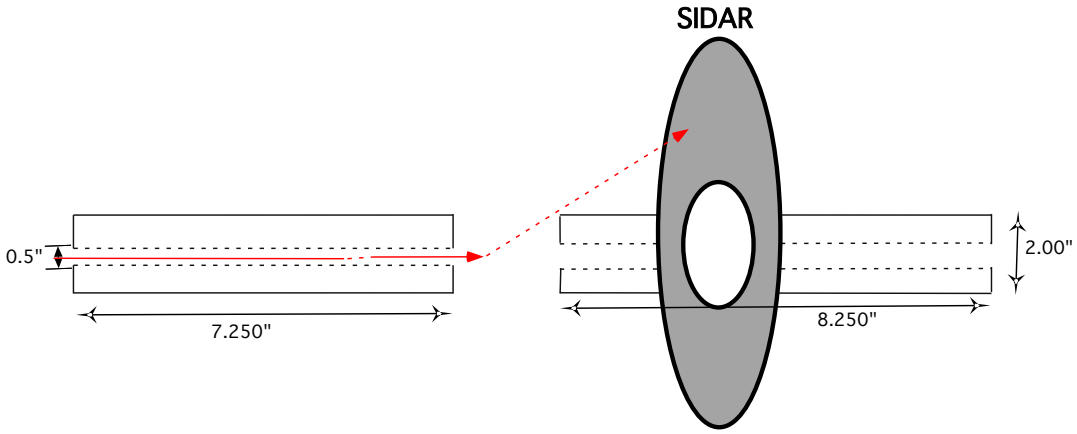

Figure 6.8: Setup proposed for the new measurement of ^{20}Ne(p, d) using a pure gas of ^{20}Ne. See text for full details.

gas targets is determining the actual point in the target at which the interaction occurred. Hence, a new setup was designed at ORNL with the capability to use a pure gas target. A schematic of the proposed SIDAR setup is shown in Figure 6.8.

In this improved setup, the target chamber will be filled with 10 Torr of a pure ^{20}Ne gas. The proton beam will travel through a narrow pipe both into and out of the chamber, though a small section of pipe near the center of the chamber will be open. In this way, the protons interacting with the gas can only be observed by the detectors in a narrow region, effectively reducing the target thickness from the length of the chamber to about a few centimeters. The exact target thickness varies with each strip since strips closer to the beam axis will have its "view" more shielded by the pipe than strips at higher angles (see Figure 6.9). Table 6.3 shows an expected count rate assuming 10 Torr of ^{20}Ne gas, a 0.1 mb cross section for the state of interest, and a beam rate of 6×10^9 pps. Here θ_{min} and θ_{max} represent the angular range covered by that strip in the laboratory frame. Currently the upstream and downstream pipes have been made and are awaiting implementation. A tank of ^{20}Ne gas has also been acquired and a system to recirculate and filter the gas is available. We look forward

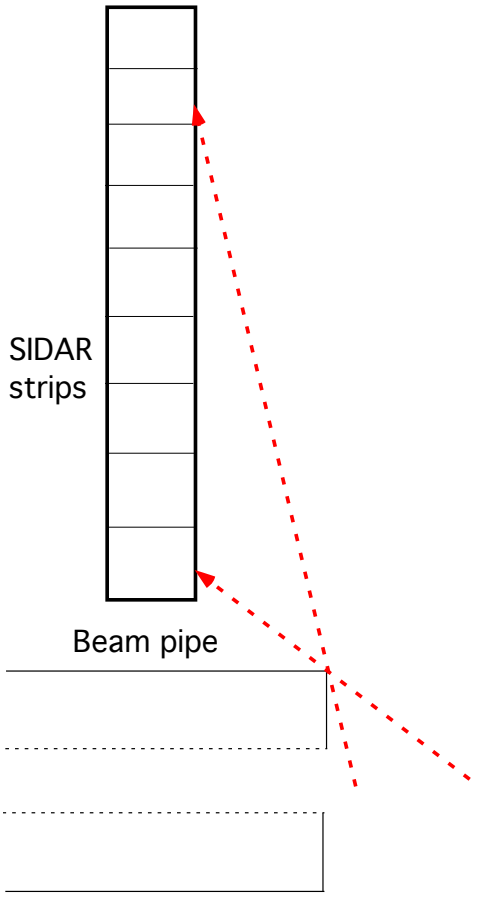

Figure 6.9: Schematic of how each strip of SIDAR sees a slightly different effective target thickness. Table 6.3 lists the effective target length of each strip.

to this measurement in the near future with the goal of determining the spin of the 6.289-MeV state in ^{19}Ne.

Table 6.3: Expected count rate and target length for the the ^{20}Ne(p, d) reaction with improved setup assuming 10 Torr of neon gas, a differential cross section of 0.1 mb/sr, and a beam rate of 6×10^9 pps.

Strip number	θ_{min}	θ_{max}	active target length (cm)	counts/hour
1	13.8	15.6	0.597	24.4
2	15.1	17.3	1.069	59.1
3	16.5	19.0	1.451	103.2
4	17.7	20.7	1.767	155.6
5	19.0	22.3	2.032	215.3
6	20.3	23.9	2.258	281.2
7	21.5	25.4	2.452	352.3
8	22.6	27.0	2.622	427.6
9	23.9	28.4	2.771	506.2
10	25.1	29.9	2.903	587.2
11	26.2	31.3	3.021	669.7
12	27.3	32.6	3.126	753.0
13	28.4	33.9	3.221	836.5
14	29.5	35.2	3.308	919.5
15	30.6	36.4	3.387	1001.5
16	31.6	37.6	3.459	1082.1

Chapter 7
Summary and Conclusions

7.1 Summary

One of the primary objectives in science is to understand the origin of elements in the universe. All of the experiments in this dissertation are part of this larger picture, and expand our knowledge of element nucleosynthesis. Each measurement of this dissertation comprises smalls steps towards achieving this goal.

7.1.1 ^{7}Be(d,d)

The ^{7}Be(d,d) measurement aimed to clarify the origin of ^{7}Li, believed to have been formed during the big bang. Currently the ^{7}Li post big bang abundance predicted by model calculations and that extrapolated from stellar observations differ by almost a factor of 4[Cyb08]. Since most ^{7}Li is produced through the beta decay of ^{7}Be, a resonant enhancement of the destruction of ^{7}Be could resolve the discrepancy. Before this measurement, resonant deuteron capture into the 16.7-MeV state in ^{9}B was regarded as a possibility whose role has been the subject of much debate [Cyb09, Ang05, Boy10]. In order to resolve the problem, the resonance would have to exist at an energy in the range 170 keV $\leq E_{cm} \leq$ 220 keV with a deuteron decay width in the range 10 keV $\leq \Gamma_d \leq$ 40 keV. At ORNL, this resonance was searched for using the $d(^7\text{Be},d)^7$Be reaction with a 10-MeV rare isotope beam of ^{7}Be and a CD_2 target. No resonance was observed. An upper limit of 1 keV was set, much lower than the smallest value required to resolve the ^{7}Li abundance problem. This possible resonance was the last proposed nuclear physics solution to the ^{7}Li abundance mystery. This study of the

^{7}Be+d reaction shows that this solution is no longer an option. Now more effort can be focused on searching for other solutions, such as the existence of the dark matter particle X^{-} which might act as a catalyst for the destruction of ^{7}Be [Kus10].

7.1.2 $^{15}\mathbf{N}(d,p)$

Currently the origins of ^{19}F are not well known, but it is believed to be produced in Asymptotic Giant Branch stars, stars with inert carbon cores with a shell of helium burning and a shell of hydrogen burning. Current models produce about 250 times less ^{19}F than is observed and efforts are being made to improve the reaction rate calculations. ^{19}F could be produced by the ^{15}N(α,γ) reaction and so any reaction that destroys ^{15}N would affect the final abundance of ^{19}F. ^{15}N(n,γ) might be one of the main channels through which ^{15}N is destroyed. Spectroscopic factors of ^{16}N are important for this reaction rate calculation and currently there is a discrepancy between measured spectroscopic factors and those expected from theory [Mei96, Boh72, Lee07]. At ORNL the ^{15}N$(d,p)^{16}$N reaction was measured to determine the new spectroscopic factors. These values were are reproduced by OXBASH theoretical prediction. This result will serve to increase the amount of ^{15}N being destroyed through the (n,γ) channel leading to a reduction of ^{19}F. Further work must be done to resolve the ^{19}F abundance discrepancy.

7.1.3 $^{20}\mathbf{Ne}(p,d)$

Electron-positron annihilation dominates gamma-ray emission from novae. The source of these positrons remains a mystery, but they are thought to originate from beta-decay of relatively abundance ^{18}F. However, no gamma-rays associated with the decay of ^{18}F have been observed. One of the reactions believed to destroy ^{18}F is ^{18}F(p,α) and much work has been done to understand this reaction rate [Ber02, Koz06, Ser07]. Work by Adekola *et al.* has shown that there is a ^{19}Ne state at 6.289-MeV just below the proton threshold that could have a substantial impact on the ^{18}F(p,α) reaction rate, but so

far its spin has not been determined [Ade11]. At ORNL, a proton beam was aimed at a carbon target implanted with ^{20}Ne in an attempt to use the ^{20}Ne(p,d) reaction to determine the spin of this state. Target contaminants made the results inconclusive. A new setup has been designed to re-measure this reaction using a pure ^{20}Ne gas target. All of the components of this setup have been received and we are waiting for beam time to carry out this measurement.

7.2 Future Detectors

The measurements described in this dissertation were made possible by the innovative detectors developed to detect the outgoing particles from each reaction. As experiments grow more challenging, further development of detectors is necessary. For example, for stripping reaction experiments in inverse kinematics, it is often the backward laboratory angles that are of interest to study. However, in this angular region, particles are often low in energy ($E < 1$ MeV) so detectors must have thresholds low enough to detect them. Furthermore, the particles of interest are often difficult to detect (i.e. low energy neutrons). With the experimental astrophysics group at ORNL, I have been aiding in the development of a new set of detectors designed to tackle some of the challenges presented by modern experimental needs.

7.2.1 Super ORRUBA

As discussed in Chapter 3, cross sections for experiments in inverse kinematics tend to peak near 90° in the laboratory frame. Detector arrays that cover angles in this region are needed in many nuclear reaction measurements done in inverse kinematics. The silicon detector array ORRUBA covers this region well and the use of resistive strips enables a large area to be covered with relatively high accuracy in θ without the need for many electronics channels. However, the use of resistive strips has several disadvantages. In order to trigger an event, a signal must be observed by both ends of the ORRUBA strip. If the particle interacts near one of the ends, the signal measured

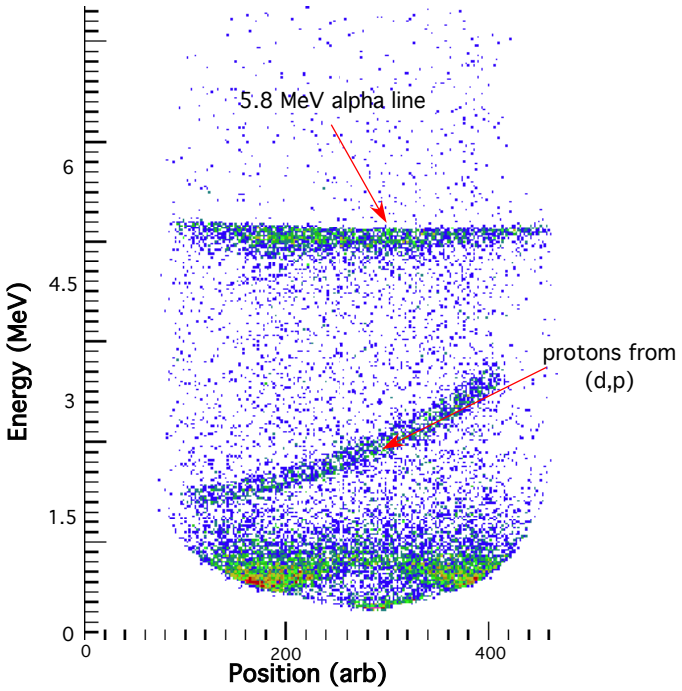

Figure 7.1: Energy as a function of position in an ORRUBA strip for the ^{15}N(d,p) measurement. Note that ORRUBA can only detect low energy protons ($E_p \leq$1 MeV) near the center of the strip.

by the other end will be weak, possibly too weak to trigger an event. This occurrence leads to a relatively high energy threshold for ORRUBA. As can be seen in Figure 7.1, only protons over 1.5 MeV in energy could be observed over the full length of an ORRUBA strip. So for measurements that would require the detection of low energy particles ($E \leq 1$ MeV), ORRUBA would not be the best instrument. Furthermore, this effect also leads to position-dependent gains in each strip. What is desired is a detector exhibiting a solid angle coverage similar to that of ORRUBA that would not have these limitations. These consideration have led to the recent efforts to develop SuperORRUBA [Pai11].

Like ORRUBA, SuperORRUBA is a silicon detector array set in a barrel configuration around 90°. However, the major difference is that rather than using resistive strips to determine θ, each detector is segmented into 64 strips along its length (see Figure 7.2). This segmentation allows for a similar angular resolution, but with a lower

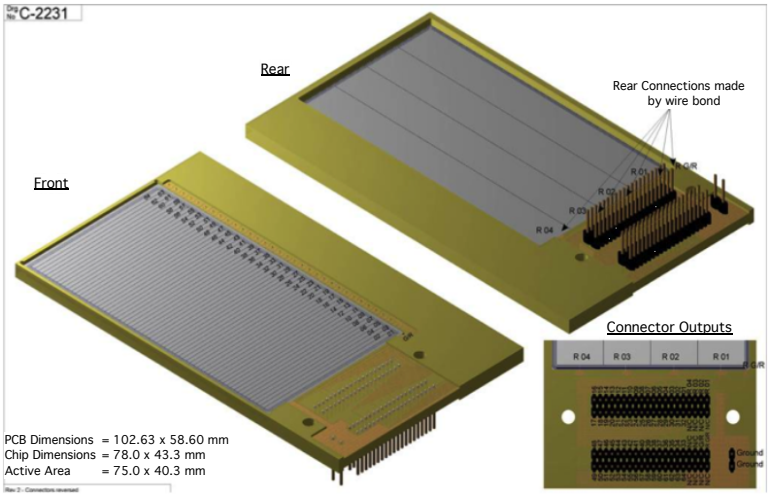

Figure 7.2: Schematic of one SuperORRUBA detector.

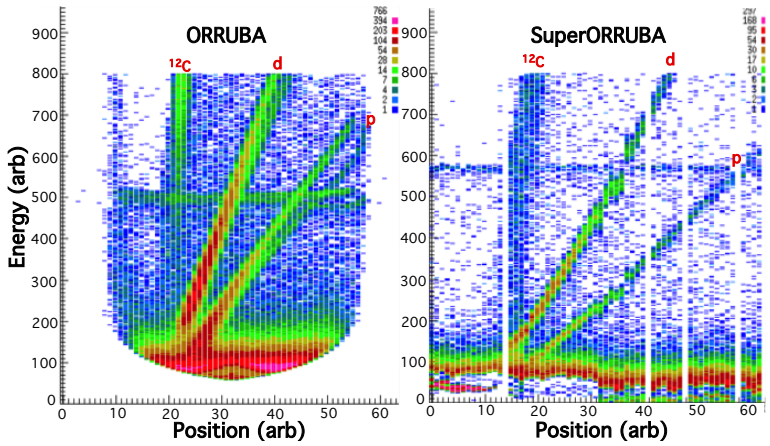

Figure 7.3: **(Left)** Energy vs position in one strip of ORRUBA. Elastic scattering from the ^{80}Ge(d,p) reaction study. **(Right)** SuperORRUBA Energy vs strip number. Notice how SuperORRUBA grants both greater energy resolution and allows the full range of the detector to be utilized for even low energy particles.

threshold. A measurement of the ^{80}Ge(d,p) reaction was done at ORNL in inverse kinematics. During this experiment, some of the differences between ORRUBA and SuperORRUBA were characterized. Figure 7.3 shows data from this measurement. Not only could SuperORRUBA observe lower energy particles (as low as 300 keV) over its whole length, it also appears as though the energy resolution has been improved because the signal is no longer being split over a resistive strip [Pai11].

7.2.2 VANDLE

The (d,p) reaction has been a useful tool for studying the properties of nuclei for decades. This statement is especially applicable to recent experiments in inverse kinematics, partially due to the fact that deuteron targets are inexpensive and relatively easy to make. Furthermore, reaction protons are emitted preferentially at backward laboratory angles where the elastic scattering does not interfere. However, the (d,p) reaction only gives us a direct measure of the characteristics of neutron levels in nuclei. In many nuclei, such as proton-rich ^{56}Ni, it is the proton levels that are more interesting for astrophysics. However, to study these levels, another tool is needed. It would also be convenient to be able to utilize similar techniques and methods as have been developed for (d,p) reaction studies. (d,n) reactions could be an excellent mirror to (d,p), but detecting neutrons is more difficult. Furthermore, since many of the nuclei of interest are unstable, these measurements would likely be done in inverse kinematics. As with (d,p), it will be important to cover the area around 90° in (d,n) studies. For this reason, the Versatile Array of Neutron Detectors at Low Energy (VANDLE) has been under development at ORNL with leadership from Rutgers University.

VANDLE incorporates two sizes of plastic detector modules so an experimental setup can be customized and tailored to its geometric and efficiency requirements. The bars of one set are shorter and thinner (3 cm x 3 cm x 60 cm), designed for the detection of neutrons in the energy range 200 keV $\leq E_n \leq$ 3 MeV. These would be arranged in an array similar to SIDAR at backward laboratory angles. A set of larger bars (5 cm

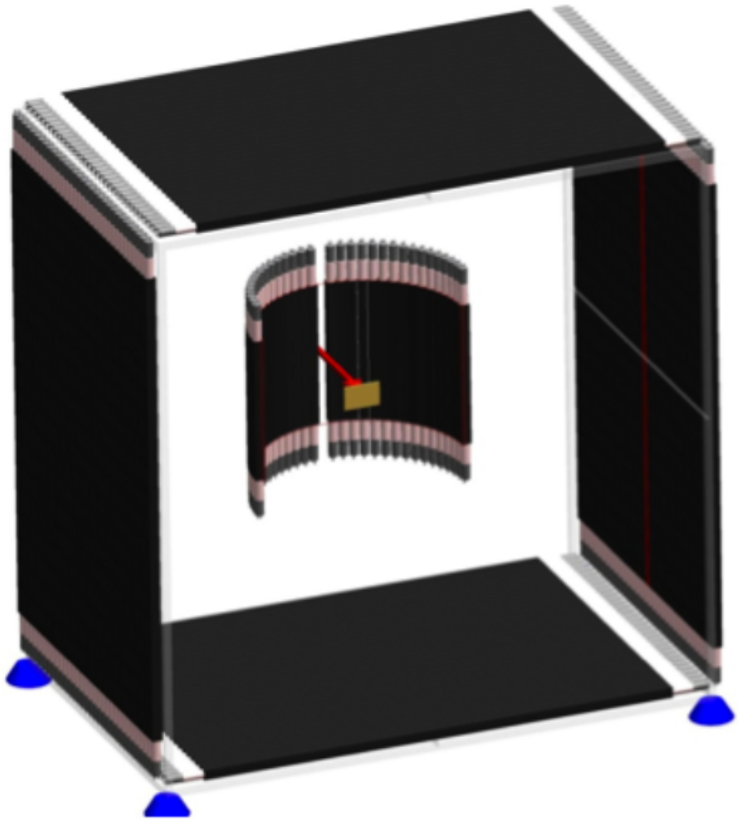

Figure 7.4: Schematic of one possible configuration for VANDLE. Shown here are the large VANDLE bars forming a box around the target analogous to ORRUBA with the smaller VANDLE bars are fit into an array around the target, similar to SIDAR.

x 5 cm x 200 cm) are designed to detect higher energy neutrons, 1 MeV $\leq E_n \leq$ 20 MeV. Every plastic scintillator bar has a photomultiplier tube coupled to each of its ends. Neutrons scatter off of the protons in the plastic, inducing light in the scintillator. Most of the light is internally reflected to the ends, but the bars are wrapped in light tight material to reflect stray light. Figure 7.4 shows a configuration of VANDLE that could be used for (d, n) measurements. Currently VANDLE has 60 small bars and 10 large bars assembled. A proposal has been approved for the National Superconducting Cyclotron Laboratory (NSCL) to measure the ^{56}Ni(d, n) reaction in conjunction with the neutron detector array MONA [Pet11].

7.3 Concluding Comments

The measurements of this dissertation are only a tiny fraction of the over all answer to the big question of how all the elements in the universe formed. A great deal of work has been done in this field and yet a great deal more is still to be done. The Facility for Rare Isotope Beams (FRIB) being built at Michigan State University will allow future researchers access to beams that have been previously out of our reach. We will be able to explore the proton and neutron driplines, which form the very edge of nuclear existence. Beyond the driplines, the nuclei will no longer be bound. Many models for nucleosynthesis require us to explore the nuclei far away from stability and understand their structure. Examples include the r-process believed to occur in supernovae where the neutron flux is so high that much of the matter in the star is very neutron-rich. Another model is the rp-process thought to occur in x-ray bursts, where the high flux of protons pushes matter towards the proton dripline. Of particular interest are nuclei around the doubly magic nuclei, such as ^{78}Ni or ^{100}Sn. Currently, studies of nuclei like these are limited by the low beam intensities available and the low cross sections ($<$ mb) for the reactions of interest. Of particular interest are reactions occurring around doubly magic nuclei such as ^{56}Ni or ^{100}Sn, where both the proton and neutron shells are closed. The next generation of facilities like FRIB will have much higher beam intensities that will allow future researchers to continue the process of gathering pieces of the larger picture of the synthesis of elements.

Bibliography

[Ang05] C. Angulo et al., Astrophys. J. **630**, L105 (2005).

[Ade11] A. S. Adekola *et al.*, Phys. Rev. C **83**, 052801 (2011)

[Bar67] A. W. Barrows, Jr., F. Gabbard, and J. L. Weil, Phys. Rev. Vol. 161 issue 4 (1967)

[Bar99] D. W. Bardayan et al., Phys. Rev. Lett. **83**, 45 (1999).

[Bar02] D. W. Bardayan et al., Phys. Rev. Lett. **89**, 262501 (2002)

[Bar11] D. W. Bardayan, private communication (2011)

[Bee11] J. R. Beene *et. al.*, J. Phys. G: Nucl. Part. Phys. **38** 024002 (2011)

[Bet37] H. A. Bethe, Rev. Mod. Phys. **9**, 69 (1937).

[Boh72] W. Bohne, J. Bommer, H. Fuchs, K. Grabisch, H. Kluge, G. Röschert, Nucl. Phys. **A196**, 41 (1972).

[Boy10] Richard N. Boyd, Carl R. Brune, George M. Fuller, and Christel J. Smith, Phys. Rev. D. **82**, 105005 (2010).

[Bra78] K. Braune, *et al.*, German Phys. Soc. **4**, (1978).

[Bru11] Carl Brune, private communication (June 2011)

[Coc04] A. Coc et al., Astrophys. J. **600**, 544 (2004)

[Cyb08] R. H. Cyburt, B. D. Fields and K. A. Olive, astro-ph/0808.2818

[Cyb09] R. H. Cyburt and M. Pospelov, astro-ph/0906.4373.

[Deo97] F. de Oliveira *et al.*, Phys. Rev. C **55**, 3149 (1997).

[For03] H. T. Fortune and A. G. Lacaze, Phys. Rev. C **67**, 064305 (2003).

[Fow67] W. A. Fowler, G. R. Caughlan, B. A. Zimmerman, Annu. Rev. Astron. Astrophys. **5**, 525 (1967).

[Her99] M. Hernanz, J. Jose, A. Coc, J. Gomez-Gomer, and J. Isern, Astrophys. J. **526**, L97 (1999).

[Her01] M. Hernanz et al., astro-ph/0103420. (2001)

[Her03] F. Herwig, N. Langer, M. Lugaro, Astrophys. J. **593**, 1056 (2003).

[How04] J. A. Howard, R. L. Kozub, J. S. Thomas, M. S. Smith, J. C. Blackmon, D. W. Bardayan, C. D. Nesaraja, Bull. Am. Phys. Soc. **49**, No. 6, 57 (2004).

[Igar] University of Surrey modified version of the code TWOFNR of M. Igarashi, M. Toyama, and N. Kishida (private communication)

[Jam88] A. N. James *et al.*, Nucl. Instrum. Meth. Phys. Res. **A267**, 144 (1988).

[Jon07] K. L. Jones *et al.*, Act. Phys. Pol. B **38**, 1205 (2007).

[Jon10] K. L. Jones *et. al.*, Nature **465**, 454-457 (2010)

[Kav60] Kavanagh, R. W., Nucl. Phys., **18**, 492 (1960)

[Koz05] R. L. Kozub *et al.*, Phys. Rev. C **71**, 032801(R) (2005).

[Koz06] R. L. Kozub et al, Phys. Rev. C **73**, 044307 (2006)

[Kra88] Kenneth S. Krane, *Introductory Nuclear Physics*, John Wiley & Sons, Hoboken, NJ. (1988)

[Kus10] Motohiko Kusakabe, Toshitaka Kajino, Takashi Yoshida, and Grant. J. Mathews, Phys. Rev. D **81**, 083521 (2010)

[Lan58] A. M. Lane and R. G. Thomas, Rev. Mod. Phys. **30**, 257 (1958).

[Lee07] D. W. Lee et al. Phys. Rev. C **76**, 024314 (2007)

[Leo87] W.R. Leo, *Techniques for Nuclear and Particle Physics Experiment*, Springer-Verlag Berlin Heidelberg New York, NY (1987)**81**, 083521 (2010)

[Loh74] J. M. Lohr and W. Haeberli, Nucl. Phys. A **232**, 381 (1974)

[Lug04] M. Lugaro *et al.*, Astrophys. J. **615**, 934 (2004).

[Mei96] J. Meissner, H. Schatz, H. Herndl, M. Wiescher, H. Beer, and F. Käppeler, Phys. Rev. C **53**, 977 (1996).

[Moa03] B. H. Moazen, R. L. Kozub, C. D. Nesaraja, M. S. Smith, J. C. Blackmon, D. W. Bardayan, J. S. Thomas, Bull. Am. Phys. Soc. **48**, No. 8, 56 (2003).

[Nel85] R.O. Nelson, E.G. Bilpuch, and G.E. Mitchell, Nucl. Inst. and Meth. in Phys. Rev. **A236**, 128 (1985).

[Nun09] Ian J. Thompson and Filomena M. Nunes, *Nuclear Reactions for Astrophysics*, Cambridge University Press, Cambridge, (2009)

[Ost07] Dale A Ostlie and Bradley W. Carroll, *An introduction to Modern Stellar Astrophysics*, Addison-Wesley San Francisco, CA (2007)

[Pai07] S. D. Pain *et al.*, Nucl. Instrum. Meth. Phys. Res. **B261**, 1122 (2007).

[Pai11] S.D. Pain, private communication (December 2011)

[Pen65] Penzias, A. A., Wilson, R. W. Astrophys. J., **142**, p.419-421 (1965)

[Per76] C. M. Perey and F. G. Perey, At. Data Nucl. Data Tables, **17**, 1 (1976).

[Pet11] William A Peters, *(d, n) studies using MoNA-LISA and VANDLE*, NSCL PAC 36 approved (December 2011)

[Pos11] Maxim Pospelov and Josef Pradler, Phys. Rev. Lett. **106**, 121305 (2011).

[Pre92] W. Press, S. Teukolsky,W. Vetterling, and B. Flannery, *Numerical Recipes*, Cambridge University Press, New York, pgs. 684-694 (1992)

[Rau94]T. Rauscher, J.H. Applegate, J.J. Cowan, F.-K. Thielemann, and M. Wiescher, Astrophys. J. **429**, 499 (1994).

[Ric05] O. Richard, G. Michaud and J. Richer, Astrophys. J. **619**, 538 (2005).

[Rol88] Claus Rolfs and William S. Rodney, *Cauldrons in the Cosmos*, The University of Chicago Press, Chicago, IL, (1988)

[Rya99] S.G. Ryan, J.E. Norris, T.C. Beers, Astrophys. J. **523** (1999)

[Rui03] C. Ruiz, *Aspects of Nuclear Phenomona Under Explosive Astrophysical, Conditions* Ph.D. dissertation, University of Edinburgh, (2003)

[Sat83] G.R. Satchler, *Direct Nuclear Reactions*, Oxford University Press, New York City, NY (1983)

[Ser07] N. de Sereville et al., Nucl. Phys. **A791**, 251 (2007).

[Ser09] N. de Sereville et al., Phys. Rev. C **79**, 015801 (2009)

[Smi98] V.V. Smith, D.L. Lambert, P.E. Nissen, Astrophys. J. **506** (1998)

[Spe03] D.N. Spergel *et al.*, Astrophys. J. **148** (2003)

[Tho05] J. S. Thomas *et al.*, Phys. Rev. C **71**, 021302(R) (2005).

[Wer05] K. Werner, T. Rauch, J. W. Kruk, Astron. Astrophys. **433**, 641 (2005).

[Wiki] *Stellar Evolution*, http://en.wikipedia.org/wiki/Stellar_evolution (January 2012)

[Wil02] S. Wilmes, V. Wilmes, G. Staudt, P. Mohr, J. W. Hammer, Phys. Rev. C **66**, 065802 (2002).

[Zie03] J. F. Ziegler, The Stopping and Range of Ions in Matter (SRIM-2003), http://www.srim.org.